DEVELOPMENT OF AlSi10Mg-AlN METAL MATRIX COMPOSITES for LASER
POWDER BED FUSION ADDITIVE MANUFACTURING

by

Jonathan Comhaire

Submitted in partial fulfilment of the requirements
for the degree of Master of Applied Science

at

Dalhousie University
Halifax, Nova Scotia
August 2023

TABLE OF CONTENTS

LIST OF TABLES

LIST OF FIGURES

ABSTRACT

AlSi10Mg is an aluminum alloy widely utilized in additive manufacturing (AM) due to its favorable response to processing and high strength-to-weight ratio. However, its stiffness, thermal conductivity, and thermal stability are insufficient for certain applications. To address these limitations, researchers have investigated the incorporation of controlled levels of ceramic particulate into the alloy. This study focuses on the influence of aluminum nitride (AlN) additions on the processability of AlSi10Mg using laser powder bed fusion. A design of experiments (DOE) approach was employed to analyze the effects of various parameters, including AlN concentration, laser power, scan speed, and hatch spacing, on the density of the final parts. The study established an effective processing window and used favorable parameter combinations to fabricate additional specimens for a comprehensive assessment of microstructure, matrix/ceramic interfaces, mechanical properties, and thermal properties.

An initial central composite design (CCD) revealed that laser power had the most significant impact on specimen density among the investigated parameters. Poor consolidation was observed when the laser power was set at or below 150W, regardless of the total volumetric energy density (VED). The occurrence of irregular lack of fusion (LOF) pores increased in terms of quantity and size outside the optimal VED range. An additional DOE demonstrated that the optimal VED range for all chemistries was 60-80 J/mm^3. However, for metal matrix composites (MMCs) with increased laser absorptivity, operating at a lower power and scan speed within this VED range could be advantageous.

A comparison between 0% AlN and 5% AlN-F specimens, fabricated using optimized tensile parameters (Laser power = 240W, scan speed = 1000mm/s, hatch spacing = 0.10mm), revealed increased gas porosity in the MMC specimens. This is attributed to the lower thermal diffusivity in the MMC powder bed, resulting in higher localized temperatures and increased vaporization. Tensile testing indicated improved elongation in the AlSi10Mg alloy following a stress-relief heat treatment, although yield strength (YS) and ultimate tensile strength (UTS) were compromised. Despite lower density, the stress-relieved MMC demonstrated YS and UTS comparable to those of the stress-relieved AlSi10Mg alloy.

LIST OF ABBREVIATIONS AND SYMBOLS USED

AB	As built
AlN-C	Coarse aluminum nitride
AlN-F	Fine aluminum nitride
AM	Additive manufacturing
AMC	Aluminum matrix composite
ANOVA	Analysis of variance
ASTM	American Standard for Testing of Materials
CAD	Computer aided design
CCD	Central composite design
CTE	Coefficient of thermal expansion
d	Layer thickness
DOE	Design of experiments
DPM	Deep-penetration melting
EBSD	Electron back scatter diffraction
EDS	Energy-dispersive x-ray spectroscopy
h	Hatch spacing
HAZ	Heat affected zone
HCM	Heat conduction melting
HIP	Hot isostatic pressing
ICP-OES	Inductively coupled plasma - optical emission spectroscopy
IPF	Inverse pole figure
L-DED	Directed energy deposition
LED	Linear energy density
LFA	Laser flash analysis
LOF	Lack of fusion
LPBF	Laser powder bed fusion
MMC	Metal matrix composite
P	Laser power

PM	Powder metallurgy
PREP	Plasma rotating electrode processing
PSD	Particle size distribution
RA	Rotary atomization
SEM	Scanning electron microscopy
SLM	Selective laser melting
SLS	Selective laser sintering
SR	Stress relief
UTS	Ultimate tensile strength
v	Laser scan speed
VED	Volumetric energy density
YS	Yield strength
ε	Elongation
ρ	Density

ACKNOWLEDGEMENTS

1. INTRODUCTION

Metal additive manufacturing (AM) is an innovative technology through which components are manufactured in a layer-by-layer manner from a metallic feedstock. These technologies are commonly referred to as "3D printing" technologies [1]. Initially conceptualized for the manufacture of rapid, non-structural prototypes, metal AM has evolved into an application capable of building unique structural components with improved characteristics over traditionally manufactured counterparts [2]. Metal AM methods are particularly interesting due to the levels of intricacy and dimensional accuracy achievable in finished components as compared to traditional processing methods, such as casting, forging, and extrusion [3], where extensive post-process machining is often required. AM technologies are capable of manufacturing materials with complex geometries [4] [5], such as walls thinner than technologically feasible through casting, and conformal cooling channels, which can be built in AM processes as a single component [5].

Sectors such as aerospace [6], automotive [7], and defence [8] have taken steps to introduce metal AM into their end products. Lightweight designs that metal AM can accommodate are beneficial in these applications to reduce weight and improve fuel efficiency. Other benefits include lead-time reduction, improved performance, and component consolidation [6].

While the benefits of metal AM as a prototyping technology have been well-established, there are still several challenges to overcome before widespread adoption of AM parts as critical components can be expected. Quality assurance is a significant hurdle as AM technologies are relatively new and all manufacturing processes must be fully understood before use for critical components [6] to avoid unpredicted failure.

Another challenge is the development and expansion of feedstock materials compatible with AM processes. A focus of AM research is to investigate powders with

characteristics compatible with AM processes and applications [9], such as laser powder bed fusion (LPBF) which is a leading metal AM technique that uses a powder feedstock.

One of the most challenging alloy systems to accommodate in metal AM is aluminum. Aluminum is one of the most widely used alloys in industry, second only to steel [10], and its alloys are of high demand in aerospace and automotive applications[5] due to its lightweight with an excellent strength-weight ratio, ductility, corrosion resistance, and electrical and thermal conductivity [11]. However, the surface oxide layer that readily forms with aluminum, which contributes to its corrosion resistance, is also a challenge in its translation to AM, due to the high melting point of the layer [5]. Additionally, the high thermal conductivity and reflectivity of aluminum alloys necessitates a higher laser energy and can invoke challenges in process robustness.

This chapter will outline the important AM technologies used in the processing of aluminum alloys. It will discuss the commercially relevant aluminum cast and wrought alloys and the development of new aluminum alloys specific to AM. This will necessitate a discussion into the challenges of accommodating aluminum alloys to AM and the research that has been done to improve the microstructure and mechanical properties of these alloys.

1.1 Laser Powder Bed Fusion AM

Laser powder bed fusion (LPBF), also referred to as selective laser melting (SLM), is a versatile AM process, successfully adapted to multiple alloy systems [2]. LPBF is a layer-by-layer process where each iteration begins with the spread of powder from a static bed onto the build surface using a re-coater. An incident laser beam then melts the powder. The laser focal point is rastered using mirrors driven by a galvanometer [2] in a pattern derived from a 3D computer aided design (CAD) model of the intended product. Through this interaction, a small melt pool forms and then rapidly solidifies as the laser moves away. The build platform is lowered by a predetermined height, allowing a new layer of powder to be spread over the surface. This sequence is repeated until the

component is built to its final dimensions. Support structures may be built concurrently with the component. Due to combustibility of some metal powders and their tendency to oxidize, the build chamber is invariably inertized. Figure 1[12] shows the configuration of a typical LPBF process.
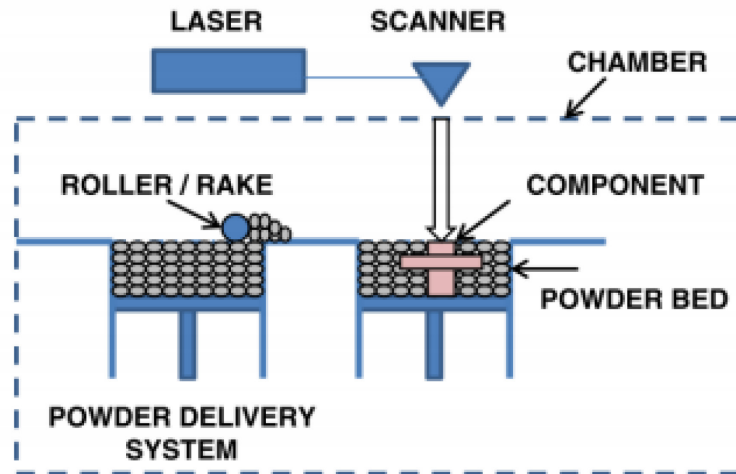
Figure 1: Laser powder bed fusion (LPBF) configuration [12]

Due to extreme localized temperatures over a small surface area, the cooling rate of the melt pool in AM is much faster than in casting. Finite element modelling has shown that an aluminum alloy melt pool experiences cooling rates of 10^6 K/s [13], compared to 10^0 - 10^2 K/s for most castings [2] and 10^2- 10^4 K/s in laser directed energy deposition (L-DED) processes [14]. As such, LPBF products exhibit finer microstructures compared to other manufacturing methods.

LPBF-manufactured parts have good surface finish and high dimensional accuracy [2]. Since parts are near net-shape and unused powder can be recycled, LPBF efficiently uses material, which can lead to savings especially with high-cost powders [5]. However, a key limitation of LPBF is build time. Relative to other metal AM processes such as L-DED and binder jetting, LPBF requires the longest build times, although multi-laser systems have been successfully introduced to market to improve build rates [3].

In LPBF, several parameters may be adjusted to optimize build properties. Table 1 [15] lists many of the processing parameters that can be adjusted, as well as the material properties that can be modified to improve processability.

Table 1: Machine and material parameters for LPBF [15]

Processing parameters	Material properties
Laser power	Viscosity
Scan rates	Surface tension
Atmospheric control	Particle size and distribution
Gas flow	Particle shape
Heaters (bed temperature)	Absorptivity/reflectivity
Laser type	Thermal conductivity
Scan radius	Specific heat
Scan vector length	Emissivity
Scan spacing	Melting temperature
Thickness of layers	Component ratio
Machine (specific type)	Chemical composition

1.1.1 Machine Parameters

Interactions between an incident laser beam and the powder bed can be classified by a series of melting modes, including heat conduction melting (HCM) and deep-penetration melting (DPM) [16]. While DPM, or "keyhole" melting, is desirable in laser processes such as welding, keyholes add to the porosity of an AM component, risking a decrease in mechanical properties. For quality assurance purposes, and to maximize mechanical properties, porosity must be minimized. In certain instances, correlations between an abundance of porosity and lower elongation to failure have been demonstrated [17], as well as a reduced fatigue strength and Young's Modulus [18].

The melting mode is dependent on the energy input to the powder bed [19], which can be described mathematically using multiple processing parameters. In one approach, laser power (P), scan speed (v), hatch spacing (h), and layer thickness (d) determine the volumetric energy density (VED) input, as per Equation 1 [20]:

$$VED = \frac{P}{vhd}$$

(1)

Subject to powder properties for each unique material, a processing window can be identified to determine process parameters that contribute to a melting mode which optimizes density. If energy density is too low, insufficient melting will cause lack of fusion (LOF) porosity, characterized by an irregular shape, due to insufficient bonding between the incident layer and the previous layer. Although mechanical properties such as ultimate tensile strength (UTS) and elongation can be maintained with small LOF pores, these properties degrade significantly as pore size increases [21]. Increases in laser power and decreases in scan speed contribute to larger melt pools and thus higher melt pool overlap and fewer LOF defects [2]. High energy densities lead to DPM and subsequent keyhole porosity [16], as well as excessive vaporization of alloying elements with low boiling points (e.g., Mg, Zn).

While VED is useful as an estimate, processing parameters within this equation have their own distinct impacts. Read *et al.* [22] studied this using a systematic approach to characterize pore formation by varying each parameter in equation (1) individually, observing that variance in laser power and scan speed had a more prevalent effect on part porosity than hatch spacing. Layer thickness is dependent on powder particle size, but typically ranges from 20-60 μm [23].

High temperature gradients between the build plate and melt surface can lead to the accumulation of thermally induced residual stresses, causing distortion within the component or sections of it [24]. Maintaining a build plate temperature can act as an *in*

5

situ stress relief, potentially to a level that reduces the need for a post-build heat treatment and/or mitigating the risk of quench cracks. However, reduction of temperature gradient, and therefore solidification rate, can lead to a somewhat coarsened grain structure and reduced mechanical properties. Buchbinder *et al*. [24], however, demonstrated that with the AlSi10Mg alloy, a common AM alloy, preheating the build plate to 250°C reduced distortions beyond detectable levels while keeping hardness greater than the requirement for die-cast parts of this alloy.

1.1.2 Powder Parameters

Powders for LPBF typically range from 10-60 μm [25] and have spherical morphology. Gas atomization is a common technique to form spherical powders from a molten metal feedstock. The degree of sphericity may be improved using atomization techniques with higher temperature gradients. Examples include rotary atomization (RA) and plasma rotating electrode processing (PREP) [2]. However, these processes come with higher costs which can be problematic as powder procurement is one of the larger factors inherent to the economics of metal AM[26].

Figure 2 [25] illustrates the key measurements that, from a material perspective, affect a powder's performance in an LPBF system. Size distribution is essential to strike a balance between flowability and detail intricacy. In this sense, fine powders have lower minimum layer thicknesses which allow for finer features but cause issues with flowability due to higher interparticle frictional forces.
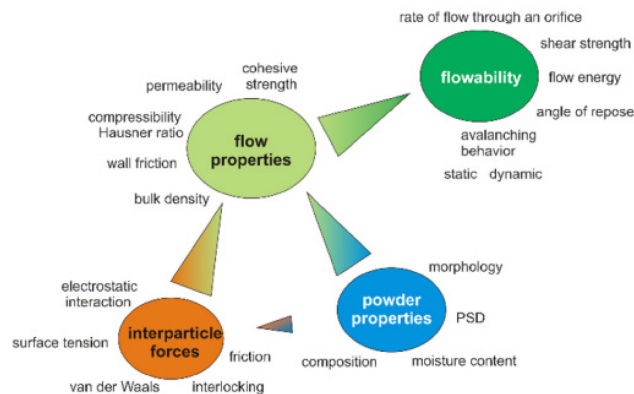
Figure 2: Key powder characteristics in LPBF [25]

6

Boley *et al.* [27] have modelled the influence of powder characteristics for a variety of metals on laser absorption of the bed in laser AM processes. Findings showed that scattering between powder particles increased laser absorptivity compared to a flat substrate of the same material. Fine powders provide a large irradiation surface area, which improves laser absorption and results in an increased melt pool temperature [28].

Powder flowability is essential in LPBF to provide a homogeneous powder surface on the build plate. Flowability is measured with a Hall Flow meter [29] or, in the case of poor-flowing powders, a Carney flow meter with a larger orifice diameter. While characterizing powders with the former is standardized for metal AM, other measurements have been proposed that may better indicate whether a powder is suitable in powder bed processes.

Spherical particles are optimal to promote flowability as irregular powder particles tend to interlock, which inhibits flow. Optimal LPBF favors a densely packed, homogeneous powder bed to reduce porosity and surface roughness [19]. In addition, an appropriate particle size distribution allows for higher packing density as fine particles fill the spaces between larger particles.

1.2 Aluminum AM

1.2.1 Aluminum Alloys in AM

Pure aluminum has advantageous properties such as corrosion resistance, ductility, and good thermal/electrical conductivity [11]. However, it is not useful in high temperature applications due to its low melting point (660℃). Several cast and wrought aluminum alloy series are prevalent in industry, some of which have been designed or repurposed to meet the specific challenges faced in aluminum AM.

1.2.1.1 Aluminum-Silicon-Magnesium Alloys

In casting alloys, aluminum is alloyed with elements that promote fluidity, high strength, and corrosion resistance [11]. Silicon is the most commonly used alloying element in

these scenarios as it improves fluidity [30] and reduces shrinkage, while concurrently lowering the coefficient of thermal expansion (CTE) [31]. Magnesium is often added to aluminum-silicon alloys to improve the strength characteristics of the alloy. However, due to the volatilization of magnesium at high temperatures [9] and its propensity to form a high melting point surface oxide [5], magnesium is typically added in small concentrations.

Most research done on AM of casting alloys pertains to AlSi10Mg. This alloy has high demand in aerospace and automotive applications due to its low density, reduced CTE, and good mechanical properties [22]. It also has a composition close to the eutectic point of the phase diagram in Figure 3 [32], which narrows the temperature range over which it solidifies. Magnesium additions (0.3-0.5%) facilitate age hardening via the formation of intermetallic Mg_2Si [33]. The microstructure of the alloy can be seen in Figure 4, with Al dendrites surrounded by a secondary phase [5]. Microstructural differences between cast and additively manufactured aluminum exist due to the difference in solidification rate. Consequences of this rate increase include finer grain sizes, reduction in dendritic growth, and increases in solid solubility of alloying elements in the aluminum matrix [34].
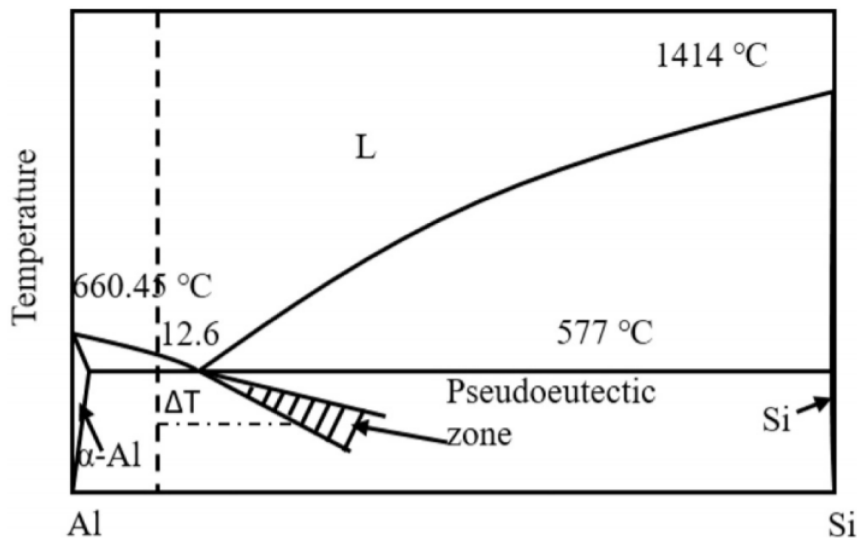
Figure 3: Aluminum-silicon binary phase diagram [32]
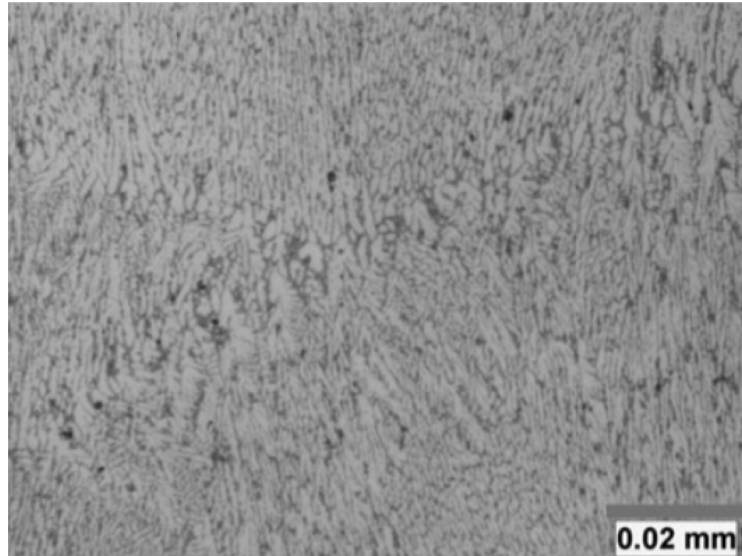
Figure 4: Microstructure of AM AlSi10Mg [5]

Figure 5 [32] is a schematic of three general zones of microstructures that form as the laser melts material in powder bed fusion of the AlSi10Mg alloy. At the top, a fine microstructure is generated due to the rapid cooling of material at the liquid-atmosphere interface. Fine, equiaxed grains are the ideal structure for strengthening due to the number of grain boundaries which resist dislocation motion and crack propagation [35], while maintaining mechanical anisotropy. In the zone below, the temperature is maintained between the solidus and liquidus temperature due to thermal conduction. Liu *et al.* theorize that these coarse zones are formed on the formation of the next layer of material when the section is heated to the "mushy zone" (between solidus and liquidus temperature). The heat affected zone (HAZ) undergoes solid state heating. This allows for the precipitation of elements out of the primary metal matrix.
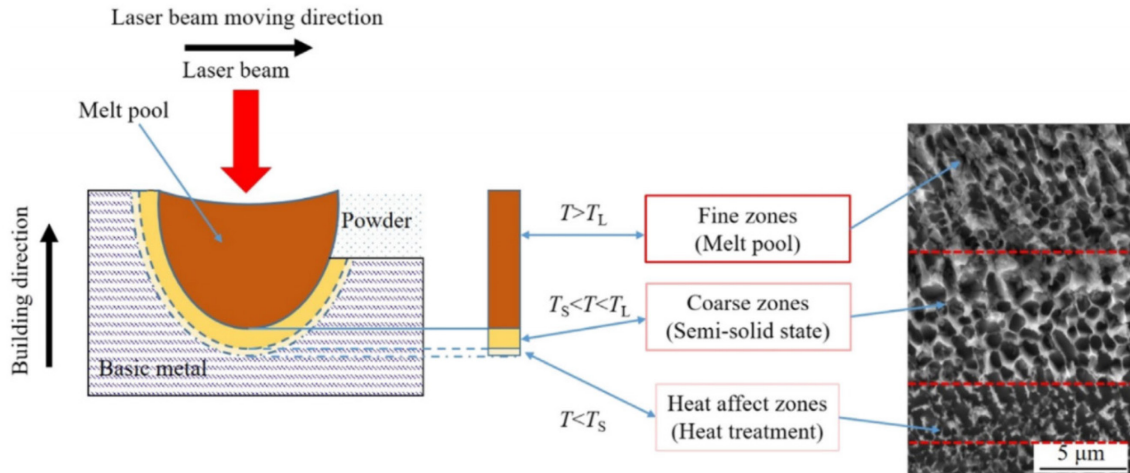
Figure 5: Microstructure as function of depth in laser melting [32]

Mechanical properties of AM AlSi10Mg alloys compared to its cast counterpart are listed in Table 2 [36]. Ductility was improved in all the additive manufactured alloys, and many had greater yield strength (YS) and UTS than the cast counterpart. Krishnan [37] investigated the effect of heat treatment, and found ductility can be increased to 12.6%, at the expense of YS and UTS. One caveat is the potential for mechanical anisotropy of AM parts leading to a difference in ductility in the longitudinal and build directions, the latter having poorer ductility [2].

Table 2: Mechanical properties of cast and LPBF AlSi10Mg [36]

Process	Reported by	Condition	Microstructure	Direction	YS (MPa)	UTS (MPa)	ε (%)
Cast	EN 1706 [38]	AB	--	--	140	240	1
LPBF	Manfredi et al. [39]	AB	Fine cellular-dendritic	Build	230 ± 5	328 ± 4	6.2 ± 0.4
				Orth. to Build	240 ± 8	330 ± 4	4.1 ± 0.3
	Krishnan [37]	HT (530℃/5h/FC)	--	–	72 ± 7	113 ± 3	12.6 ± 0.9
		T4	--	–	131 ± 9	227 ± 4	6.9 ± 0.8
		T6	--	–	245 ± 8	278 ± 2	3.6 ± 0.8
	Schmidtke et al. [40]	AB	--	–	275	340	8
	Kempen et al. [41]	AB	Al cells/dendrites decorated with Si	Build	–	396 ± 8	3.47 ± 0.6
				Orth. to Build	–	230 ± 5	5.55 ± 0.4
	Read et al [22].	AB	--	Build	250	340	1.3
				Orth. to Build	230	315	1.05
	Buchbinder et al. [42]	AB	Dendritic	Build	--	360	--
				Orth. to Build	--	420	--

In LPBF, thermal stresses are introduced by rapid solidification from the high temperatures induced by laser melting [43]. As such, stress-relief heat treatments are used to improve ductility in AlSi10Mg AM parts. However, the temperature for stress relief must not reach the alloy's recrystallization temperature and can have negative effects on UTS. In other situations, the build plate may be heated to reduce the thermal gradient. While this can lessen residual stress, it is not eliminated from the manufactured components.

Table 3 [44] lists the typical tensile properties of AlSi10Mg following common heat treatment cycles. In the as-built (AB) state, UTS and YS are maximized but ductility, or elongation (ε), is poor. Stress-relief (SR) is performed by heating to 285°C and holding for 2 hours, allowing for reallocation of stresses, resulting in increased elongation at the expense of YS and UTS. T6 heat treatment can have a transformational effect on the dendritic microstructure of AlSi10Mg, where the fine microstructure is lost and a globular second phase of silicon is formed [5]. Hot isostatic pressing (HIP) combined with a T6 treatment (solutionizing heat treatment at 530°C for 6 hours, water quenched, and aged at 160°C for 6 hours) [44], can improve ductility.

Table 3: Typical finished part properties for AM AlSi10Mg specified by ASTM International [44]

Material Condition	YS (MPa)	UTS (MPa)	ε (%)
AB	413	220	4
SR	241	138	10
T6	345	207	5
HIP + T6	276	207	10

1.2.1.2 Aluminum-Silicon

Another common casting alloy that has been effectively translated to AM is AlSi12, an alloy that solidifies very close to the eutectic composition of the Al-Si binary (11.7% Si). Figure 6 [45] shows three micrographs of an AlSi12 AM microstructure, increasing in magnification. In a), the laser raster path can be seen, as well as melt pool boundaries formed during building. On the right, the microstructure is most refined due to the high solidification rates in LPBF. Along the grain boundaries, silicon rich areas with an elongated cellular structure are visible [36], these areas being the last to solidify with the most grain growth. Marola *et al.* showed that specimens solidified via LPBF had silicon solid solubility up to 4 at % in aluminum compared to other rapid solidification processes such as copper mold casting (2 at %) and melt spinning (1 at %) [46]. This result shows

the potential increases in strength possible due to solid solution strengthening higher than typically possible in casting processes. Table 4 [36] shows a similar increase in mechanical properties for the AlSi12 alloy as seen in Section 4.1.1 with the AlSi10Mg alloy.
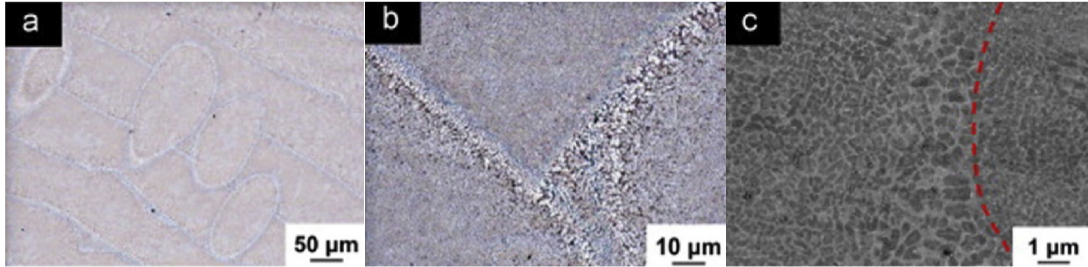
Figure 6: Microstructure of LPBF-processed AlSi12 when viewed at increasing magnifications [45]

Table 4: Mechanical properties of cast and LPBF AlSi12 [36]

Process	Reported by	Condition	Microstructure	YS (MPa)	UTS (MPa)	ε (%)
Cast	EN 1706	As-Cast	Eutectic	130	240	1
LPBF	Prashanth *et al.* [45]	AB	Cellular σ-Al w Si at Boundaries	260	380	3

1.2.1.3 Aluminum-Copper

Copper is another strengthening element added to these alloys which does not vaporize at relatively low temperatures. Aluminum-silicon-copper casting alloys have also been investigated for AM purposes, specifically AlSi9Cu3 [47]. This alloy is used in automotive applications due to its excellent strength-weight ratio, as well as its weldability and castability [48]. Figure 7 compares the mechanical properties of this alloy along the x-direction (a) and the z-direction (b) with various heat treatments. The anisotropy of the microstructure only has a significant impact on the ductility, while the yield strength and UTS are unaffected. The graph also shows how heat treatment can be used to improve the ductility of the AlSi9Cu3 alloy [5].

13
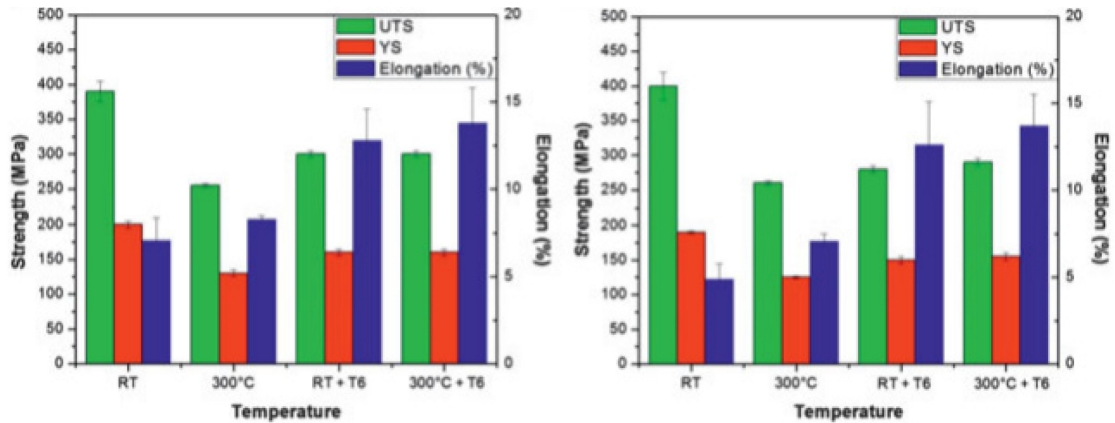
Figure 7: Mechanical properties of AlSi9Cu3 alloy in the a) x-direction and b) z-direction [5]

Aeromet has developed the A20X alloy series based on the aluminum-copper system. Aluminum-copper alloys have higher strength than aluminum-silicon alloys, but are not widely used due to their poor casting characteristics [11] [49]. A20X is a cast alloy compatible with AM and has YS and UTS greater than Al 6061 and comparable with Al7075 [50]. The alloy contains an addition of titanium diboride [51], a hard ceramic often used as a grain refiner. TiB_2 restricts the movement of liquid into the interdendritic channels [49], which improves the alloy's susceptibility to solidification cracking as discussed in Section 3.3. An increased addition of titanium leads to refinement of the grain size. Figure 8 shows the effect of elemental titanium on the grain size of the A20X alloy. The additional titanium leads to the formation of $TiAl_3$, a more effective grain refiner than TiB_2 [49]. After heat treatment, the AM A20X alloy exhibits excellent mechanical properties including 440Mpa YS, 511 MPa UTS, and 13% elongation [51].
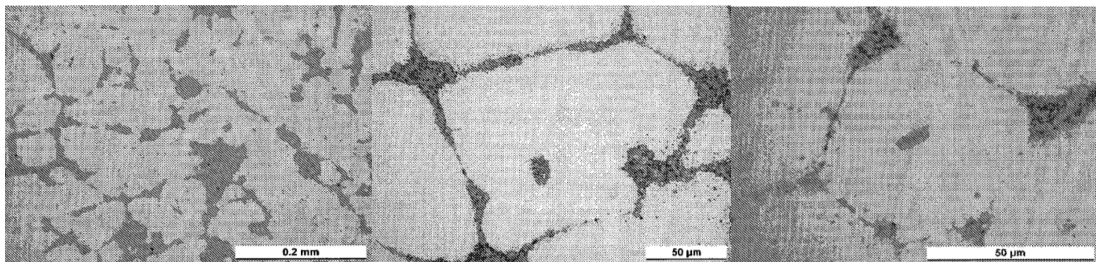
Figure 8: Microstructure of A20X alloy with increasing Ti addition: a) 0.02wt%, b) 0.15wt%, c) 0.17wt% [49]

14

Aluminum wrought alloys are generally grouped into two classifications: heat-treatable and non-heat-treatable. This section will focus on the former, as they are a more viable option for potential applications that rely on elevated mechanical performance [5].

Heat-treatable wrought alloys include the 2XXX series (Al-Cu-Mg), 6XXX series (Al-Si-Mg), and 7XXX series (Al-Zn-Mg-Cu) [5]. All are strengthened through precipitation hardening whereby the alloy is quenched to form a supersaturated solid solution and raised to an intermediate temperature, at which time hard intermetallic precipitates are formed within the matrix [35]. These precipitates act as barriers to dislocation motion and give these alloys excellent strength.

However, many widely used high-strength alloys such as Al 6061 and Al7075 are challenging in the context of LPBF AM. Since LPBF is similar, in essence, to a welding process, materials suitable for AM are generally limited to those that are weldable [4]. Heat-treatable wrought alloys often have wide solidification temperature ranges and are susceptible to solidification cracking. Additionally, strengthening elements magnesium and zinc can evaporate during AM due to the large necessary energy inputs, leaving porosity in the material and significant changes in material chemistry.

To improve the solidification properties of these alloys, silicon has been added to increase the fluidity and shorten the solidification range of Al7075 [31]. Silicon addition is effective in reducing the crack density and also increases the laser absorption of the alloy, while still allowing for precipitation hardening of the strengthening phases [31].

Another method of combating solidification cracking is the formation of fine, equiaxed microstructures. Martin *et al.*[4] propose the addition of nanoparticle grain refiners to create nucleation sites ahead of the solidification front, reducing the undercooling required to form a fine, equiaxed grain structure. Zirconium nanoparticles were used to promote the formation of the Al_3Zr phase [4]. Figure 9 shows the effect of the addition of

zirconium on the rate of solidification and on the resulting microstructure of Al7075. While the solidification behaviour remains unchanged, the new microstructure is free from cracks. Table 5 compares mechanical properties between Al7075 + Zr and traditionally manufactured Al7075, as well as additive manufactured AlSi10Mg. Although the mechanical properties were not as high as wrought Al7075, the method shows that traditional alloys with higher strength than the common AM alloys can be manufactured, albeit with lower ductility [4].
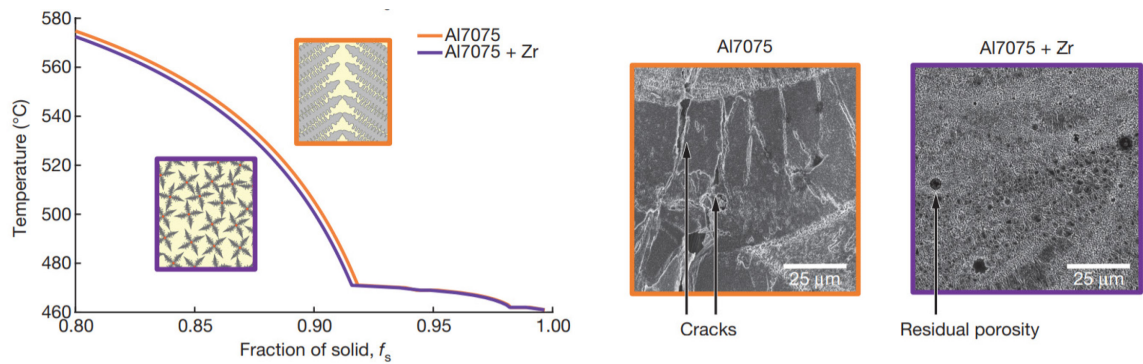
Figure 9: Comparison of solidification path and resulting microstructure of Al7075 and Al7075 with Zr addition [4]

Table 5: Mechanical properties of wrought and AM Al7075 and other AM alloys [4]

Material	YS (MPa)	UTS (MPa)	ε (%)
AM Al7075 (T6)	NA	25.5	0.4
Wrought Al7075 (T6)	372-469	462-538	3-9
AM Al7075 + Zr (T6)	325-373	383-417	3.8-5.4
AM AlSi10Mg	209	315	7.3

Another additively manufactured alloy that utilizes transition metals is Scalmalloy, an aluminum-magnesium-scandium alloy. Scalmalloys are corrosion resistant and have high strength and high ductility [5]. In this alloy, an Al_3Sc phase acts as a grain refiner upon solidification, and heat treatments can improve the hardness of these alloys [5]. Al_3Sc precipitates can be formed through a quenching and aging process. This phase is coherent with the aluminum matrix and remains thermally stable up to 350°C, a value that greatly exceeds the stability threshold of Mg and Cu-based precipitates. [31].

Scalmalloys have excellent mechanical properties as shown in Table 6 [31]. Prior to heat treatment, Scalmalloy has similar mechanical properties to AlSi10Mg. However, post-build heat treatment significantly increases the YS and UTS, while maintaining similar levels of ductility. This data shows the benefits of developing heat-treatable alloys that are compatible with AM. Unfortunately, the high cost of scandium ensures that Scalmalloys may be cost prohibitive for certain applications.

Table 6: Mechanical properties of AM AlSi10Mg and Scalmalloys [31]

Material	Heat Treatment	YS (MPa)	UTS (MPa)	ε (%)	Source
AlSi10Mg	AB	270	460	9	[52]
AlSi10Mg	SR	230	345	12	[23]
Scalmalloy	AB	276-287	403-427	14-17	[53]
Scalmalloy	325 deg C 4h	520	530	14	[40]

1.2.2 Challenges in Aluminum AM

1.2.2.1 Raw Powder Traits

For a powder to be compatible with LPBF, several basic traits are of concern. One is that the powder must have good flowability. This is necessary to form an even layer preventing defects within the finished product. Aluminum and its powders, however, often have poor flowability due to its lighter weight compared to other metals such as titanium and steel [54]. In addition, fine powder can agglomerate and bridge during the spreading process which can lead to an uneven layer thickness and porosity within the final part.

Table 7 compares the flowability, as well as the thermal conductivity and reflectivity, of a series of AM powder feedstocks. Notably, the AlSi10Mg powder tested by Aboulkhair [54] has no measured flowability using a Hall flow meter by ASTM standard B213 [54][29]. However, flow properties of a feedstock are influenced by particle size, morphology, moisture content, and a variety of other factors [55]. To optimize flow characteristics, spherical aluminum alloy powders should be used, as irregular particles tend to impede flow.

Table 7: Properties of steel, titanium, and aluminum AM powders [54]

SLM Candidate Material	Flowability (s/50g)	Thermal Conductivity (W/m K)	Reflectivity (%)
Ti64	47	6.7	53-59
316L Stainless Steel	14.6	21.4	60
Al 6061	77	172	91
AlSi10Mg	No flow	146	91

Thermal conductivity and reflectivity of a powder are other traits of influence. Such data for several materials are presented in Table 7 where Al6061 (high-strength aluminum alloy) and AlSi10Mg are compared to Ti-64 and 316L stainless steel. Aluminum alloys have higher reflectivity and thermal conductivity, therefore requiring a higher energy input to enable melting [5]. Rapid dispersion of input heat leads to an increased solidification rate [56] and lowers melt pool stability. Aluminum also readily forms an oxide with a high melting point. Consequences of incomplete melting include pores and defects within the material from which cracks can be initiated [5].

Insufficient energy density inhibits fusion, causing porosity within the part. If, when building a layer, the previous layer is not re-melted, the two layers will not have coherent bonding [10]. Insufficient energy density can also cause a balling effect, where the molten metal forms highly concentrated areas of material in the melt pool [5]. The balling effect can increase surface roughness and induce porosity in the product, and, in extreme cases, the balls can interfere with powder deposition [57]. Figure 10 shows the impact of increasing linear energy density on the cross-section of an AlSi10Mg single scan track [58].
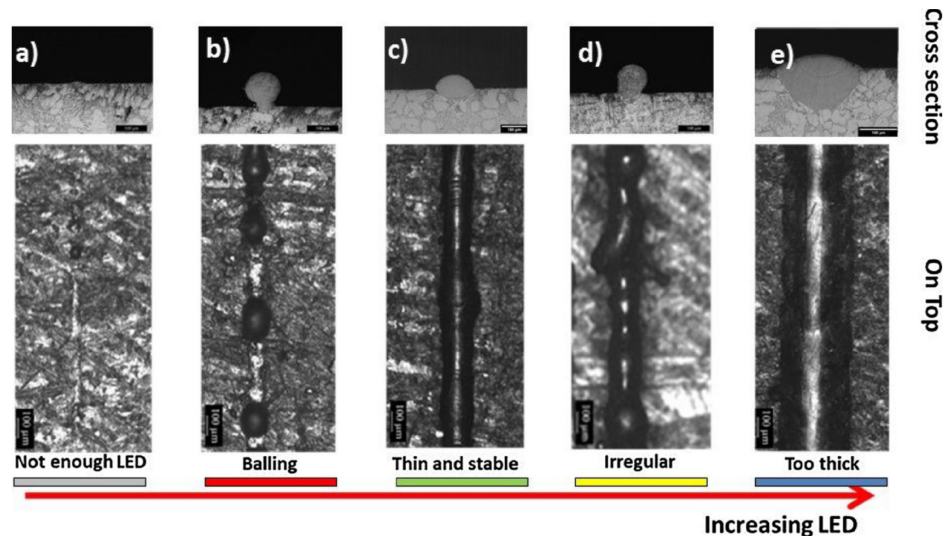
Figure 10: Effect of increasing linear energy density on balling phenomena for an AlSi10Mg single track [58]

The energy density required for complete melting of the substrate and prevention of the balling effect can lead to the volatilization of low vapor pressure alloying elements (zinc, magnesium, etc) commonly used in high-strength aluminum alloys [9]. Martin *et al.* [4], in an attempt to manufacture Al 7075 through LPBF, noted that the process resulted in a 25% loss of zinc and 32% loss of magnesium, both of which are strengthening elements in the alloy. For this reason, many of these high-strength alloys are challenging to process via AM without adverse modifications to the alloy chemistry.

Additionally, the high thermal conductivity of aluminum can lead to melt penetration of pre-built layers when the energy density is too high (low scan speed, high laser power) [31]. This creates defects that have a "keyhole" shape, as alloying elements can vaporize due to the high energy input and leave voids in the already built layers. This porosity can increase the risk of crack growth within the sample during solidification and reduce the yield strength and density of the final part.

1.2.2.2 Solidification Cracking

Solidification rates are multiple orders of magnitude higher in AM processes than in casting [4]. Aluminum has a high CTE and thus, a high rate of solidification shrinkage [5] upon cooling as well. Shrinkage can interfere with dimensional accuracy in AM if not

accounted for and often leads to cracking if the stress associated with shrinkage is too high in the presence of a solidifying liquid and/or stress concentration points such as voids within the material.

Aluminum alloys, especially heat-treatable high strength alloys, are susceptible to solidification cracking. The mechanism of solidification cracking is the entrapment of liquid between solidified regions. When the alloy solidifies, the equilibrium phase solidifies before the bulk liquid, causing a solute enrichment at the solid-liquid interface. The molten metal is trapped as the material solidifies, and the newly solidified material undergoes dendritic growth in the direction of the laser path [4]. The molten metal is trapped between layers and the tensile stress that these voids are under leads to tearing.

A factor that determines the degree of dendritic grain growth is the temperature range over which solidification occurs. Figure 11 [4] compares the dendritic growth of AlSi10Mg and Al7075, the former with a solidification temperature range of approximately 30°C [31] and the latter with a range of 175°C. The long dendrites formed in the solidification of the 7075 alloy leave small voids which can act as stress concentrators for crack formation.
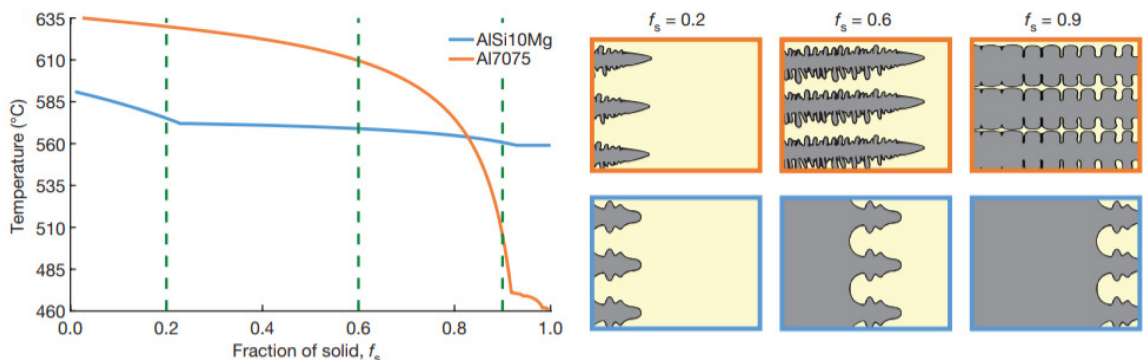
Figure 11: Dendritic growth of AlSi10Mg and Al7075 alloys during solidification [4]

1.2.2.3 Mechanical Anisotropy

In LPBF, the direction of grain growth correlates with build direction [2]. Grain size and orientation differ in the longitudinal and transverse directions, and this difference leads to anisotropy, or directionality, of mechanical properties such as YS, UTS, and elongation.

Anisotropy can be reduced by alternating laser scan path [33], but this is limited to the directions perpendicular to the build direction. Differences in grain size and dimension with an alternating scan path can be observed in Figure 12 [32].
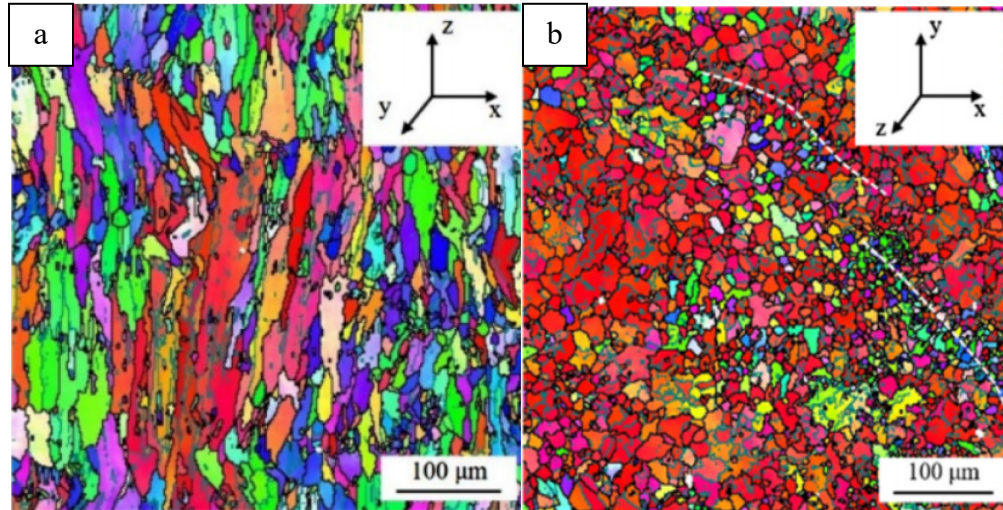
Figure 12: Electron back scatter diffraction (EBSD) inverse pole figure (IPF) maps of AlSi10Mg at P=325W, oriented in a) the build direction and b) the y-direction [32]

As with the previous challenges to aluminum AM, alloys with large solidification temperature ranges suffer most due to the long columnar grains that grow in the coarse grain zone [32]. Contraction is greatest in the build direction, leaving the part most susceptible to cracking in this direction [2]. An experiment by Fulcher *et al.* [59] measured the mechanical properties of Al6061 built using LPBF. Specimens showed significantly lower UTS in the longitudinal direction (42 MPa) compared to the transverse direction (230 MPa). This disparity shows the unsuitability of these alloys in components with multi-directional stresses [2].

1.3 Aluminum Matrix Composites

Metal matrix composites (MMCs) are multiphase materials consisting of a reinforcement material within a pure metal or metal alloy matrix [35] [60]. Typically, the reinforcement is a material with higher strength and hardness than the metal matrix, such as a ceramic [35]. Common examples include carbides, nitrides, oxides, and borides [61]

MMCs are desirable in automotive and aerospace applications due to increased service temperature and excellent properties [61]. Specifically, aluminum and its alloys are used in these applications due to their corrosion resistance and high strength-weight ratio [11]. However, aluminum's overall mechanical properties compared to other metals and metal alloys, limits usage in certain applications. These disadvantages can be mitigated via reinforcement with a ceramic material with good mechanical and thermal properties.

While there are already widely utilized methods of processing MMCs, there is potential for these materials to be fabricated using AM methods such as LPBF. With the same processing techniques used to produce aluminum matrix composite (AMC) feedstocks for powder metallurgy, powder could also be used in AM to manufacture parts that are easily customizable, have excellent dimensional tolerance, and near-net shape, requiring little post-process machining. Aluminum alloys with ceramic additives are commercially available and have mechanical properties on par with high-strength aluminum alloys that have been deemed unprintable.

This section will discuss the strengthening mechanisms of ceramic reinforcements within the metal matrix, as well as the processing methods used to manufacture these materials. AMCs and their applications will be discussed, as well as the aluminum-ceramic combinations that have translated well to AM.

1.3.1 Discontinuously Reinforced Composites

Ceramic reinforcements exist in particulate, fibre (either continuous or discontinuous), and whisker morphologies. Since this thesis focuses on the viability of aluminum MMCs

in AM from a powder feedstock, the focus will be on strengthening mechanisms of discontinuous reinforcement particles.

In particle reinforced MMCs, fine particles of a hard, inert material that is insoluble in the metal matrix[35] are uniformly dispersed. This subtype of MMC is defined by reinforcement particles with an aspect ratio less than 5 [62]. Micro or nanoscale ceramic particles exhibit greater strength than bulk ceramics [60]. The strengthening mechanism is similar in nature to precipitation hardening, in that small particles act as barriers for dislocation motion. Particulates carry an additional load that eases stress on the matrix, while also forming incoherent interfaces between the matrix and particulates, which result in the generation of dislocations at these interfaces [63]. While the magnitude of the strengthening effect is lower, dispersion strengthening can be advantageous over precipitation hardening in that over-aging is not a factor since the composite is more stable at high temperatures than a precipitation hardened counterpart [35].

Compatibility between matrix and reinforcement phases is essential. One factor of utmost importance is the difference in CTEs, as mismatches can lead to accumulation of strain [61], which can affect the composite [64]. The magnitude of thermally induced residual stress is dependent on factors such as ceramic particle size, aspect ratio, and volume fraction [62].

The interfacial region is significant since the interaction between matrix and reinforcement determines load transfer and crack resistance [61]. Figure 13 shows the failure mechanisms that can occur within a MMC [65]. With a high strength matrix such as an aluminum alloy, the load can be shifted to the particulates until a point where cracking can originate within the particles. For a pure aluminum MMC, failure can occur at the matrix-particle interface resulting in decohesion between the two phases [60].
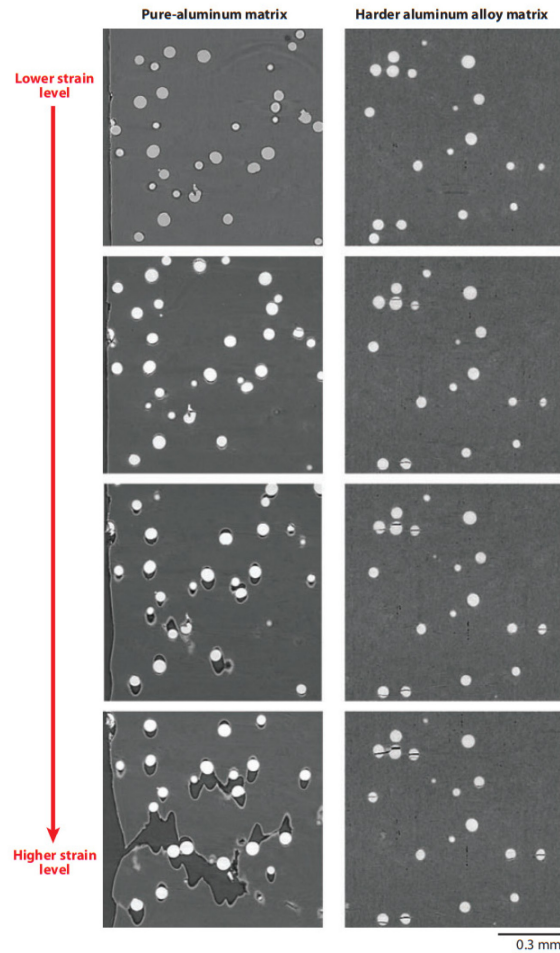
Figure 13: Failure mechanisms in MMCs [65]

Addition of ceramic particulate also impacts the solidification structure of MMCs [62] by acting as a catalyst for heterogeneous nucleation. For a ceramic to act as a nucleation site, the particle must exhibit good wetting properties with the molten metal [66]. When molten metal wets poorly to ceramic particles, particles rejected by the solidifying front of the metal segregate to the interdendritic regions which solidify last, leading to non-uniform distribution and poor mechanical properties as a result [66][67].

1.3.2 Conventional Processing Methods

1.3.2.1 Stir Casting

When casting a MMC, consistent stirring is essential for prevention of particle agglomeration [60] [68] and settling [61]. Stir casting is a common processing method for

MMCs, as stirring action allows for high volume fractions of particulates with good bonding between the matrix and reinforcement phases [63]. Increased temperatures (>900°C) improve wettability of particulates to the molten metal [69], which is necessary to maximize interfacial bond strength [61].

Figure 14 shows a schematic diagram of a stir casting apparatus. Parameters such as stir time and process temperature [69] can be optimized to improve the effectiveness of mixing.
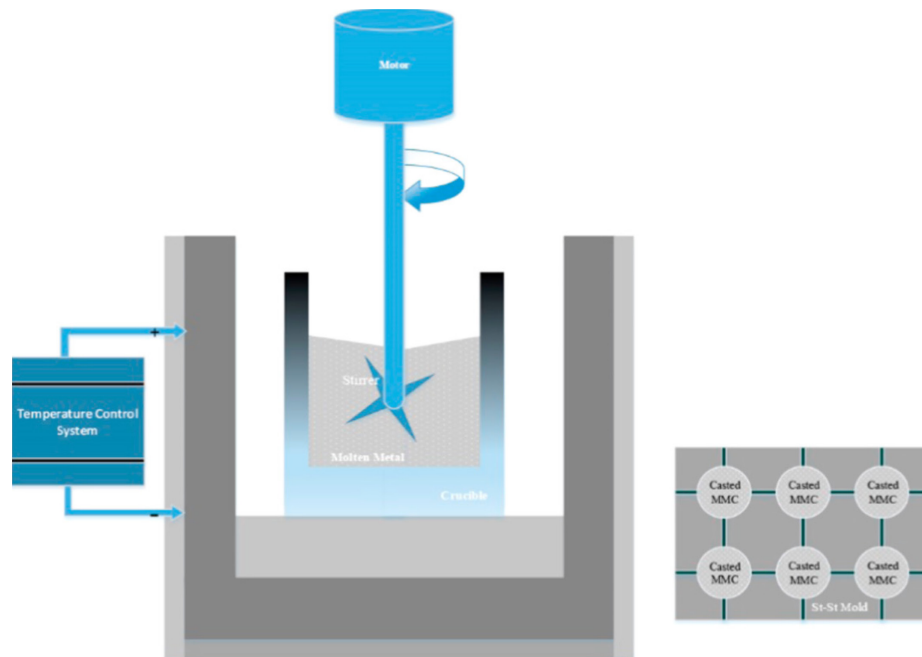
Figure 14: Stir casting schematic [69]

1.3.2.2 Pressure Infiltration

Pressure infiltration, or squeeze casting [63], is another liquid phase method of MMC processing. Here, molten alloy is injected into a porous ceramic preform via a mechanical device or inert gas [61] and as pressure increases, liquid metal is forced into a chamber with the preform reinforcement [70]. Figure 15 shows a schematic of a system where the required pressure is provided by inert argon gas [70]. In this device, an insulating, porous

layer separates the molten metal from the ceramic preform and upon infiltration, the pressure difference drives the molten metal into the cooled preform.

This processing technique is simple, fast, cost-effective [1], and can accommodate volume fractions of ceramics up to 50% [71], but the ranges of shapes and sizes are limited by the shape of the preform and the process can cause damage to the reinforcement matrix [61] [71].
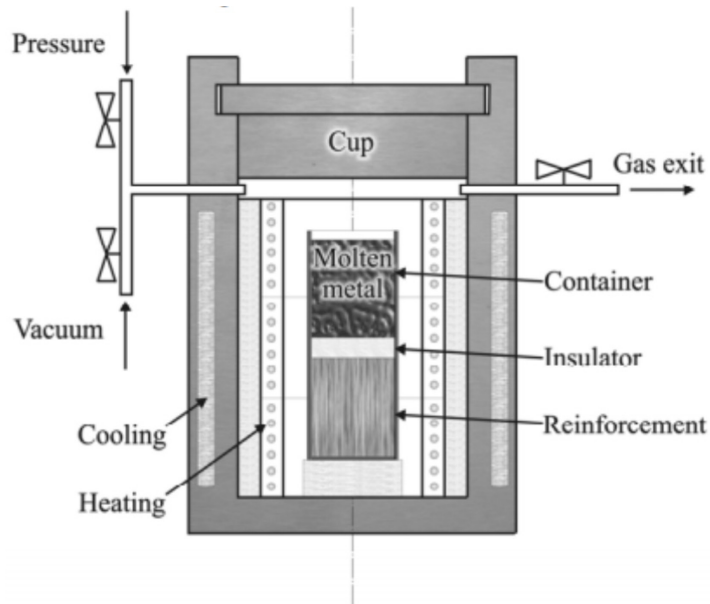
Figure 15: Pressure infiltration casting apparatus [70]

1.3.2.3 Powder Metallurgy

Powder metallurgy (PM) is a solid-state process. This allows for manufacturing at low temperatures, reducing the potential for negative interfacial reactions between the reinforcement and matrix [72]. PM techniques are effective in forming a part with a uniform distribution of reinforcement, a requirement to enhance material strength [72].

Powder feedstocks are fabricated using techniques such as milling, electrolytic production, and water and gas atomization [73]. Atomized powders are most advantageous due to their spherical shape allowing for improved flowability, especially for aluminum and aluminum alloys that generally have poor flowability [54]. Figure 16 shows one example of a PM process flow chart from feedstock powder to a finished

component [72]. In the attrition phase, metal and ceramic parts are combined by mechanical alloying, a solid phase process where an alternating process of breakdown and welding of individual particles is used to form an alloy [74]. High revolution speed is necessary to generate the required heat for particle recombination [73]. Figure 17 shows scanning electron microscopy (SEM) images for two initial powders (gas atomized V95 aluminum alloy and SiC), and the resultant powder after mechanical alloying in an attrition mill. Large granules that form due to combination of the aluminum and silicon carbide powders begin to attrite [74].
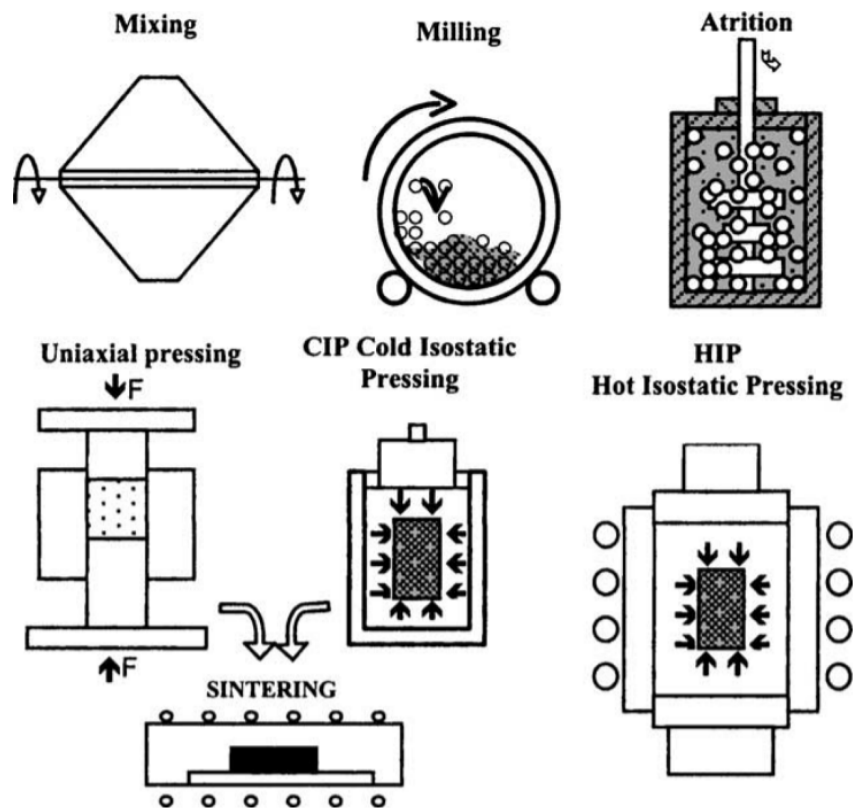
Figure 16: PM process flow chart [72]
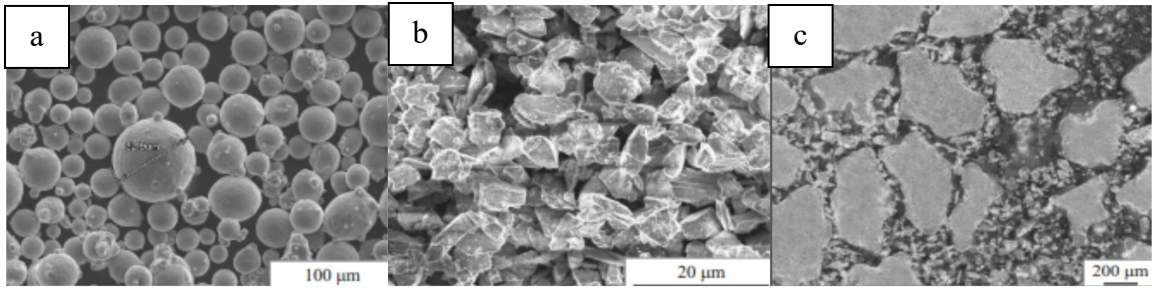
Figure 17: Powder morphology of a) V95 Al alloy, b) SiC, and c) both powders mechanically alloyed for 2.5h to produce a combined microstructure [74]

1.3.3 Applications of AMCs

Aluminum is an established matrix metal in MMCs, owing to its low density [61]. There is significant demand for light, high-strength materials in automotive [63] and aerospace industries, as well as sectors such as agriculture and mining [63]. Weight reduction is essential in improving fuel economy and efficiency and combining the properties of aluminum with a ceramic can improve the strength and modulus of aluminum while maintaining its low weight. Other beneficial properties seen in AMCs include excellent wear resistance, corrosion resistance, high temperature creep resistance, reduced CTE, and improved fatigue strength [75]. Table 8 shows the effect of increasing addition of Al_2O_3 and SiC on the YS, UTS, elongation, and modulus of common aluminum alloys [3]. Naturally, as the strength properties are increased through addition of reinforcements, elongation of the alloy decreases.

Table 9 [76] outlines current applications of aluminum MMCs in the automotive industry. Components such as crankshaft bearings and engine blocks [63] can be made from AMCs, reducing the overall weight of the vehicle and improving fuel economy. Another usage of AMCs in the automotive industry is the replacement of cast iron brake disks, which can reach high operating temperatures. Figure 18 shows a brake disk made from particle reinforced aluminum, a composite with high wear resistance necessary for use in this application [63].

Table 8: Mechanical properties of Duralcan AMC alloys [3]

Alloy	Yield Strength (MPa)	UTS (MPa)	Elongation (%)	Modulus (GPa)
6061-0% Al2O3	276	310	20	69
6061-10% Al2O3	297	338	7.6	81
6061-15% Al2O3	386	359	5.4	88
6061-20% Al2O3	359	379	2.1	99
2014-0% Al2O3	414	483	13	73
2014-10% Al2O3	473	517	3.3	84
2014-15% Al2O3	476	503	2.3	92
2014-20% Al2O3	483	503	0.9	101
A356 - 0% SiC	200	276	6	75
A356 - 0% SiC	283	303	0.6	81
A356 - 0% SiC	324	331	0.3	90
A356 - 0% SiC	331	352	0.4	97

Table 9: Automotive applications of AMCs [76]

Manufacturer	Composite	Component
Duralcan, Martin Marietta, Lanxide	Al/SiC	Pistons
Duralcan, Lanxide	Al/SiC	Brake rotors, calipers, liners
GKN, Duralcan	Al/SiC	Propeller shaft
Nissan	Al/SiC	Connecting rod
Dow Chemical	Mg/SiC	Sprockets, pulleys, covers
Toyota	Al/Al2O3	Piston rings, (saffil) & AI/Boriaw
Dupont, Chrysler	Al/Al2O3	Connecting rods
Hitachi	Cu/graphite	Current collectors
Martin Marietta	Al/TiC	Pistons, connecting rods
Honda	Al/Al2O3-C	Engine blocks
Lotus Elisse, Volkswagen	Al/SiC	Brake rotors
Chrysler	Al/SiC	Brake rotors
GM	Al/SiC	Rear brake drum for EV-1, driveshaft, engine cradle
MC-21, Dia-Compe, Manitou	Al/SiC	Bicycle fork brace, disk brake rotors
3M	Al/Nextelf	Missile fins, aircraft electrical ac door
Knorr-Bremse, Kobenhavn	SiC/Al	Brake disc on ICE bogies
Alcoa Innometalx	Al/SiC	Multichip electronic module
Lanxide	Al/SiC	PCB heat sinks
Cerecast	Al/graphite foam	Electronic packages
Textron	Al/B	PCB heat sinks
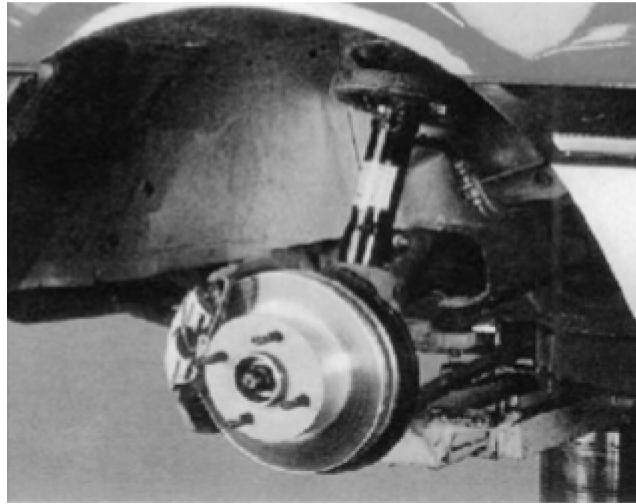
Figure 18: Automotive brake disk comprised of particle reinforced aluminum [63]

1.3.4 AMCs in AM

Traditional methods of processing MMCs are often limited to simple designs [1] or require extensive post-process machining. Due to the hardness of MMCs, high strength tool steels are required for machining, which can introduce significant costs [77]. An alternative to the traditional processing methods is AM, where the component is built through the continuous addition of thin layers of powder. AM technologies can produce intricate designs with near-net shape, reducing machining costs while increasing efficiency of material usage. Additions of ceramic powder to an aluminum alloy may also aid in the printability of these alloys by improving the energy absorptance of the powder bed [1].

Figure 19 [78] outlines several *in situ* and *ex situ* techniques for AM of MMCs. *Ex situ* MMCs are either blended or mechanically alloyed to the desired composition outside of the manufacturing process (or, in the case of DED, from different input feeds), while for *in situ* composites, ceramic structures are the result of reactions between elemental powders initiated by the high energy inputs required for AM. Selection between an *ex situ* and *in situ* process is a balance between simplicity and cost. Elemental powders are

less expensive than alloyed powders, but *in situ* processing can be complex, as the necessary reactions are exothermic and must be controlled.
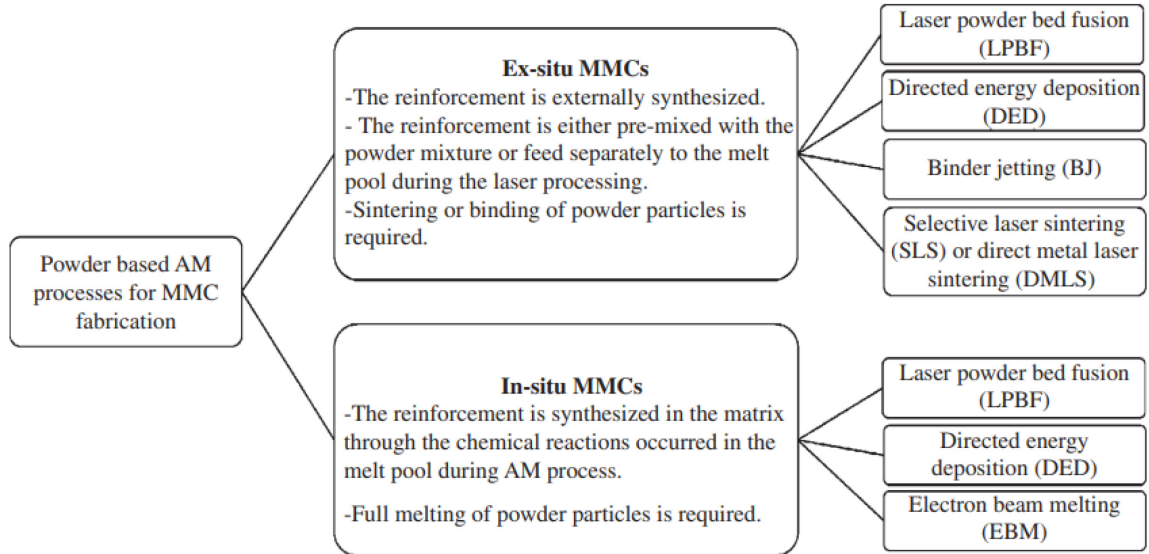
Figure 19: Powder-based AM processes for MMCs [78]

1.3.4.1 AMC Research for AM

Aluminum-silicon alloys, while commonly utilized in metal AM, have lower strength than heat-treatable wrought aluminum alloys, limiting their use in certain high-stress applications without the addition of a strengthening phase. Famodimu *et al.* [77] proposed that the addition of silicon carbide could be a suitable ceramic additive for reinforcing aluminum alloys. To achieve the necessary distribution of SiC, AlSi10Mg and SiC powders were mechanically alloyed. Figure 20 shows the microstructures of AlSi10Mg AM alloys with 0%, 5%, and 10% silicon addition, respectively. The matrix alloy has a typical structure of AM alloys. In the melt pool region, there are two distinct regions of dendritic aluminum and a eutectic Al+ Si phase. In the HAZ, dendrites are longer due to the slower cooling rate in this region [77] and thus, this area undergoes a heat treatment as the next layer is built [32].
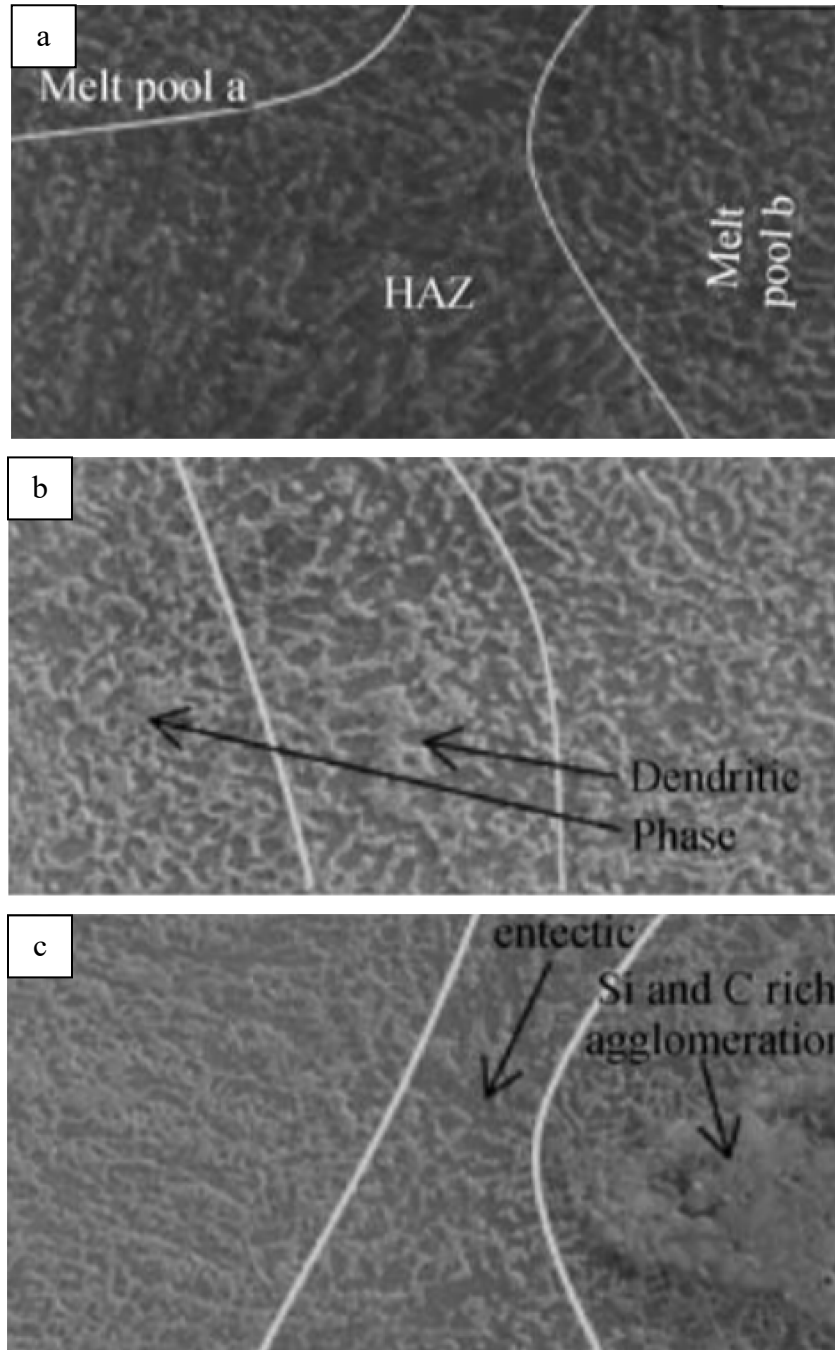
Figure 20: Microstructures of a) matrix alloy AlSi10Mg, b) AlSi10Mg-5%SiC, and c) AlSi10Mg-10%SiC, 20000x magnification [77]

As the SiC content increases, dendrites begin to coarsen due to the increased time required to achieve solidification [77]. At 10% SiC, there is a clear formation of a region enriched in silicon and carbon (bottom image) caused by the preferential formation of aluminum carbide precipitates in the eutectic phase [77]. While fine particles of Al_4C_3

can increase the strength of aluminum alloys [79], the formation of this compound to the detriment of SiC negatively impacts the mechanical properties of the composite [80].

1.3.4.2 Commercial Alloys

Elementum 3D, a research and development company that specializes in AM, has utilized a technique called reactive AM to introduce ceramics into AMCs. Using this methodology, input materials react to form products in situ, resulting in a part with phases of different chemistry than its input powders [81]. This method differs from typical methods of MMC processing in that the ceramic particulates aren't expected to be inert. The heat generated from an exothermic reaction allows the reaction to propagate through the sample. This reaction must be controlled to prevent a negative effect on the detail and tolerances of the component [81]. Products of this reaction can include both ceramics and intermetallics if the reactant is a ceramic of a different metal, such as TiB_2 or TiC. Reinforcement powder can be added both as a blend with metal powder or coated on the aluminum powder by spray drying or mechanical alloying. When the powder is blended, these materials should be similar in size to the aluminum alloy particles [81].

Table 10 shows the effect that the addition of 10% ceramic has on the mechanical properties of Elementum's A1000 alloy, which is a near-pure aluminum with small concentrations of impurities manufactured using LPBF [82]. Addition of the ceramic not only significantly increased the important mechanical properties but reduced the thermal conductivity of the alloy as well, which improved the density of the aluminum alloy. Since many high-strength aluminum alloys are unprintable using LPBF due to wide solidification temperature ranges, it is promising that good mechanical properties were achievable for an additively manufactured alloy.

Table 10: Comparison of mechanical, physical, and thermal properties of Elementum's A1000 alloy series [82]

Property	A1000 Alloy	A1000 MMC (10% ceramic)
Density (g/cm3)	2.7	2.91
Relative Density (%)	>99.5%	>99.99%
UTS (MPa)	100-110	343
YS (MPa)	76-83	262
ε (%)	30-36	--
Hardness (HRB)	--	55
Modulus of Elasticity (GPa)	70	93
Thermal Conductivity (W/m*K)	217	108

Another company innovating in AMCs for AM is Aeromet. Aeromet's A20X alloy, designed as a casting alloy, is an aluminum-copper alloy compatible with AM. The alloy contains an addition of intermetallic titanium diboride [49], a hard ceramic often used as a grain refiner. Nanoparticles of titanium diboride occupy interdendritic regions and act as nucleation sites, improving the solidification characteristics by reducing the potential for hot tearing [4] [49].

Table 11 compares the A20X AM alloy with high strength, traditionally processed heat-treatable aluminum alloys 6061 and 7075 [51]. The A20X alloy has higher strength than Al6061 and lower strength than Al 7075, putting it in the realm of high strength alloys for aerospace and automotive applications while also being printable using LPBF.

Table 11: Mechanical properties of A20X AM alloy vs. wrought Al6061 and Al7075 alloys [51]

Alloy	YS (MPa)	UTS (MPa)	ε (%)
Al 6061 Wrought Alloy T6	275	310	17
Al 7075 Wrought Alloy T6	503	572	11
A20X AM Alloy T6	440	511	13

2. RESEARCH OBJECTIVES

Through past collaborations with GKN Powder Metallurgy, the processing of AMCs with admixed aluminum nitride (AlN) additives have been researched at Dalhousie University through conventional powder metallurgical technologies such as press-and-sinter and sinter-forge [83], [84]. These studies have demonstrated that AlN additions can offer gains in mechanical performance relative to the unreinforced alloy matrix system without any adverse impact on processing behaviour. As such, these AlN-reinforced AMCs are now utilized in the high-volume fabrication of a growing list of automotive components including planetary carriers and gear pumps. The over-arching objective of this work was to build upon these developments by investigating the fundamental processing response of AlN-reinforced AMCs in the context of AM. Here, the effects of AlN additions on the LPBF processing response of aluminum alloy AlSi10Mg have been considered.

Using a design of experiments (DOE) approach, the laser power, scan speed, and hatch spacing build parameters were systematically varied. The effects of each individual parameter, as well as the effect of volumetric energy density (VED) were examined across AMCs with different concentrations and sizes of particulate additive through a series of DOEs. All products were then characterized to assess the density, general microstructure, and basic mechanical properties (hardness, tensile) alloy matrix was also investigated.

3. FABRICATION OF AlSi10Mg-AlN METAL MATRIX COMPOSITES USING LASER POWDER BED FUSION TECHNOLOGY

J. Comhaire[1], I.W Donaldson[2], D.P. Bishop[1]

1- Department of Mechanical Engineering, Dalhousie University, Halifax, NS, B3J 1Z1, Canada

2- GKN Powder Metallurgy, Auburn Hills, M, 48326, United States

Abstract: AlSi10Mg has evolved to become a standard aluminum alloy utilized in additive manufacturing (AM), owing to a robust response to processing and desirable properties such as a high strength-weight ratio. Despite these promising traits, the stiffness, thermal conductivity, and thermal stability of AM AlSi10Mg remains inadequate for certain applications. In an effort to bolster performance in these areas, coupling the alloy with controlled levels of ceramic particulate is under investigation. Specifically, the authors have completed research on the incorporation of aluminum nitride (AlN) additions and how these influence the processability of AlSi10Mg in the context of laser powder bed fusion. Using a design of experiments (DOE) approach, the effects of AlN concentration, laser power, scan speed, and hatch spacing on final part density were studied. With an effective processing window established, positive combinations of parameters were utilized in the fabrication of additional specimens needed for a comprehensive assessment of microstructure, matrix/ceramic interfaces, mechanical properties, and thermal properties.

Keywords: laser powder bed fusion, additive manufacturing, aluminum, metal matrix composites

3.1 Introduction

Metal additive manufacturing (AM) technologies have been utilized to manufacture "near net shape" components [31] that have tight dimensional tolerances [2] and generally require minimal post-process machining. Other advantages include a capacity for rapid customization and prototyping, light weighting, and efficient use of high-cost materials [5]. Laser powder bed fusion (LPBF) is a particularly common AM process, where metal powder feedstock is fed from a powder reservoir to the build area using a coater. Thinly laid powder is then melted using a laser, in a pattern derived from a 3D computer aided design (CAD) file. Once the laser is rastered, the platform is lowered, and a fresh layer of powder is spread. Repetition of this pattern in a layer-by-layer manner results in a finished component. Microstructurally, LPBF components are renowned for their fine

microstructures owing to the rapid solidification rates (10^6 K/s) [13] inherent to laser melting.

Adaptation of certain high-strength aluminum alloys to metal AM technologies has been challenging due to the rapid solidification conditions. Over a wide temperature range for solidification, an undercooled liquid phase forms near the solid-liquid interface [4]. As the material solidifies and experiences dendritic grain growth, the liquid phase can become entrapped in the interdendritic regions. Thermal contraction in these regions can then initiate cracks that can propagate through the material [85]. Additionally, the high reflectivity and thermal conductivity inherent to aluminum typically necessitate the use of a high laser power for adequate melting [10].

Alternatively, lower strength aluminum-silicon alloys have been extensively studied for use with AM technologies, owing to their high fluidity and narrow solidification range in light of their near eutectic composition [5]. One of the most studied of these alloys is AlSi10Mg [22]. Several studies have been conducted to determine the processing window that optimizes density for AlSi10Mg [16], [22], [86] in terms of laser power, scan speed, hatch spacing, layer thickness, and other parameters.

LPBF parameters and energy density for a series of parametric analyses and other studies centered around the AlSi10Mg alloy are listed in Table 12. Parametric analyses by Read *et al.* [22] and Hyer *et al.* [86] observed the relative density response to LPBF parameters of laser power, scan speed, hatch spacing, and layer thickness. These studies were able to achieve the highest density products when the input volumetric energy density (VED) ranged from 32-67 J/mm^3. While this basic parameter has limitations [87] and different researchers may have varying optimal values for the same alloy based on the constituent values for power, scan speed, hatch spacing, layer thickness, VED still serves as a useful design parameter when seeking to achieve a dense final product.

Table 12: LPBF parameters for AlSi10Mg used in process optimization studies.

Laser Power (W)	Scan Speed (mm/s)	Hatch Spacing (μm)	Layer Thickness (μm)	Build Plate Temperature (°C)	Optimal VED (J/mm^3)	Max Relative Density (%)	Source
100-200	700-2000	200-800	30	Not Reported	60	99.2	[22]
150-350	100-10000	90-170	30-90	100	32-54	99.8	[86]
200	1400	105	30	Not Reported	45	99.4	[33]
250	500	150	50	30, 300	67	> 99	[88]

While AlSi10Mg has a robust response to processing, its strength is still inadequate for certain applications [89]. To bolster the performance of these alloys, aluminum matrix composites (AMCs) have been investigated for LPBF processing [77][90], [91]. AMCs combine positive attributes of aluminum, such as toughness and ductility, with the heightened modulus, hardness, and strength of ceramics [77]. Ceramic additives contribute to strengthening due to grain refinement, leading to Hall-Petch strengthening, as well as the Orowan effect as particulates act as barriers to dislocation motion [90]. Additionally, certain ceramic particulate additions have been demonstrated to improve the laser absorption of the AlSi10Mg powder bed; namely, SiC and TiB$_2$ [92].

In several studies, parametric analyses have been implemented to optimize the as-built density of Al-based composites [77] [90] [91]. In one, Astfalck *et al.* examined the LPBF response of Al12Si-SiC MMCs fabricated with energy density between 20-80J/mm^3. A peak relative density of 97.4% theoretical was achieved and the formation of byproducts (Al$_4$C$_3$ and primary Si) were observed at higher energy densities [91]. Famodimu *et al.* optimized densification with scan speeds ranging from 720-880mm/s in AlSi10Mg composites with 5% and 10% SiC addition [77]. Aversa *et al.* investigated AlSi10Mg composites with additions of micro and nano TiB$_2$ and MgAl$_2$O$_4$, achieving near full

densification with the nano-scale powders, although poor distribution was observed due to Marangoni flow interactions with the nanoparticles [90].

Another potential ceramic additive is AlN. This ceramic has high strength, low CTE, and good wetting properties with molten aluminum [93]. While research on AlSi10Mg-AlN composites have been completed [94] [95], these studies primarily focused on modelling melt spread behaviour and melt pool thermodynamics. Dai *et al.* were successful in fabricating AlSi10Mg-1% nano-AlN composites using LPBF, observing good distribution and grain refinement, leading to improved wear resistance properties [94]. However, studies that emphasize a parametric analysis of the LPBF build parameters for this specific AMC system are seemingly absent from the open literature. To address this knowledge gap, this work seeks to establish a processing window for the LPBF of AlSi10Mg-AlN AMC systems that contain different concentrations and types of AlN additions using a DOE-based approach.

3.2 Materials

Gas atomized AlSi10Mg powder produced by Kymera International was utilized as the matrix alloy in this study. This feedstock was sieved to a range from 20-63 µm by the supplier, a range that was confirmed using a HELOS laser diffraction particle measurement system. Chemical composition data acquired using a combination of inductively coupled plasma - optical emission spectroscopy (ICP-OES) and inert gas fusion techniques are listed in Table 13.

Table 13: AlSi10Mg powder chemical composition (weight %).

% Si	% Mg	% O	% Al
10.1	0.39	0.12	Balance

Two grades of AlN produced by H.C. Starck were utilized in this study. The particle size distribution (PSD) of each powder was measured by laser light scattering (Malvern Mastersizer 3000) as shown in Figure 21. These powders are denoted as AlN-C (coarse) and AlN-F (fine) in this study given their respective differences in average particle size.

The D_{10}, D_{50}, and D_{90} for both grades of AlN as well as the AlSi10Mg powder are listed in Table 14 while SEM images of the metal and ceramic powders are shown in Figure 22. The AlSi10Mg powder had a spherical morphology typical of a gas atomized powder, with satellite formation noted in some instances. Both ceramic powders had an angular morphology, but the AlN-C exhibited a broader size range and larger average particle size.
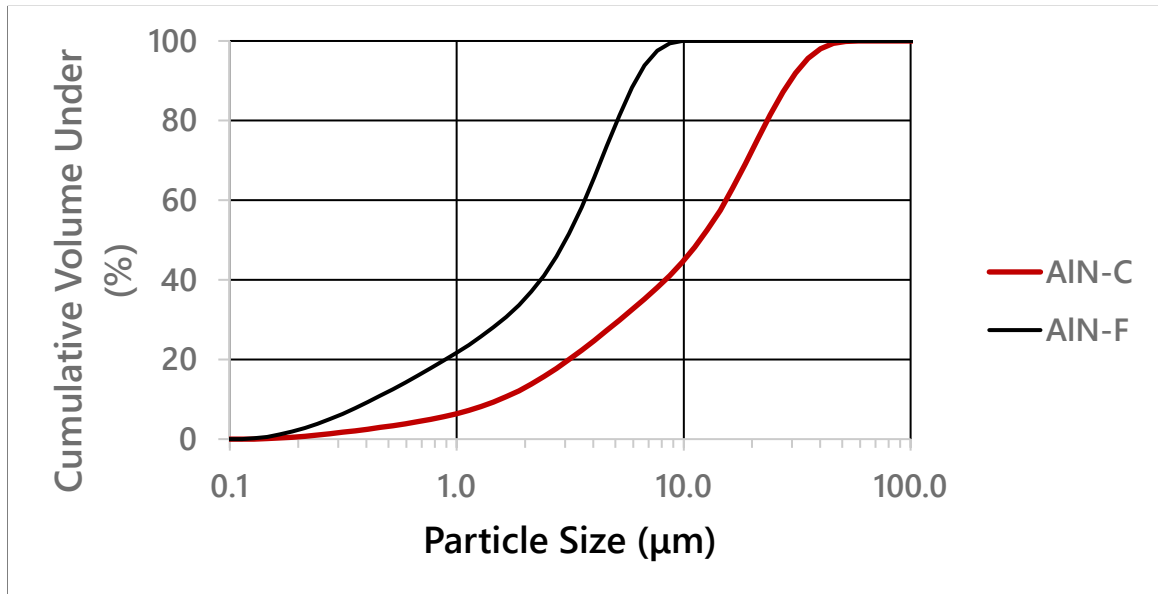
Figure 21: Particle size distributions of AlN-C and AlN-F
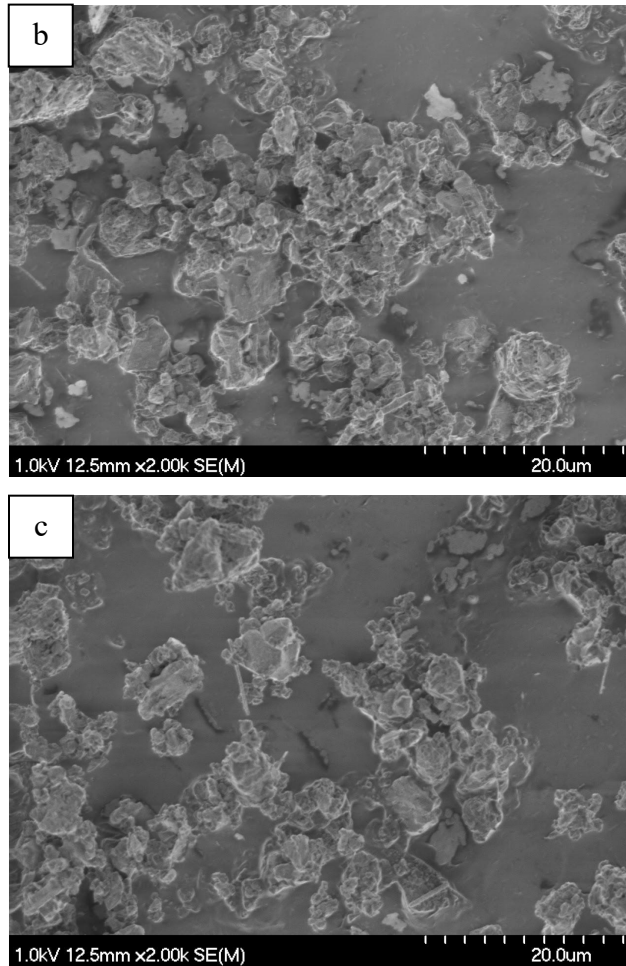
Figure 22: SEM images of (a) AlSi10Mg powder, (b) AlN-C, and (c) AlN-F.

Table 14: Particle size data for feedstock powders.

Material	D_{10}	D_{50}	D_{90}
AlSi10Mg	22.1 μm	39.4 μm	64.0 μm
AlN-C	1.6 μm	11.8 μm	29.5 μm
AlN-F	0.4 μm	3.0 μm	6.2 μm

Several AlSi10Mg/AlN mixtures were considered in the work. This included the base material devoid of AlN (hereafter referred to as 0%AlN), and others that admixed AlN-C or AlN-F particulate. These systems are denoted as 5%AlN-C, 10%AlN-C, and 5%AlN-F with all percentages indicating the weight % of AlN added. In each case, the required

amounts of feedstock powders were blended using a Turbula Model T2-F powder mixer with a residence time of 1 hour. An approximate value for the full theoretical density of each blend was determined by means of helium pycnometry (Micromeritics AccuPyc II 1340 Pycnometer). Each blend was assessed 10 times and average values calculated. Flowability of each system was measured using a Carney flow meter. While the development of measurements that measure "spreadability" for an AM context have been researched [96], flow rate can be used as a predictor due to the similarity in physical processes which occur in both flow and spreading [97]. The composite blends with AlN-C additions did not flow through the orifice of the flow meter, indicating that spreadability could be poor in the LPBF process.

Thermal diffusivity was measured using a NETZSCH LFA427 laser flash analysis (LFA) apparatus and analyzed using NETZSCH Proteus software. Data on these basic physical traits are shown in Table 15.

Table 15: Basic physical characteristics of powder blends.

Powder Blend	Flow Rate (s/50g)	Full Density (g/cm^3)	Thermal Diffusivity (mm^2/s)
0%AlN	13.8	2.65	0.359 ± 0.021
5%AlN-C	No flow	2.68	0.184 ± 0.009
5%AlN-F	37.4	2.68	0.324 ± 0.010
10%AlN-C	No flow	2.71	0.183 ± 0.028

3.3 Methodology

Samples of each MMC system were fabricated by means of LPBF using an AconityMini system (Figure 23) equipped with an ytterbium fiber laser (400 W max power, 1.07µm wavelength, Gaussian energy distribution). Layer thickness, spot size, and build plate temperature were all held constant at 0.03mm, 0.08mm and 220°C, respectively. A meander scan strategy was utilized with 90° rotation between layers. To limit oxidation, all builds were executed under a high purity argon atmosphere. The measured oxygen concentration was < 50 ppm in all instances. Powder was spread using a silicone blade

that was vibrated at a fixed ultrasonic frequency of 180 Hz. Arrays of cuboidal specimens were printed as shown in Figure 24.

Figure 23: Aconity 3D LPBF machine utilized for all builds.

TOP VIEW   FRONT VIEW

Y

Z   X

N   N + 1

(a)

Powder
Flow

Gas
Flow

14 cm

(b)

47
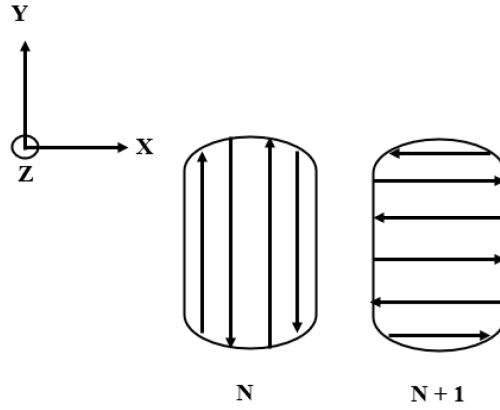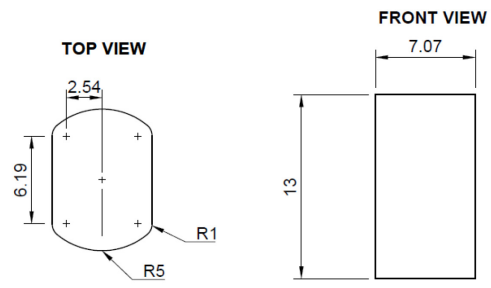
(c)

Figure 24: Schematics of the (a) cuboidal specimen geometry with scan strategy and the build plate configurations utilized in (b) DOE-1 and (c) DOEs 2-3. Dimensions cited are in mm.
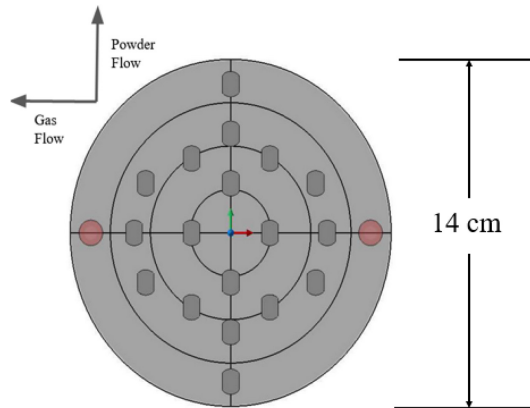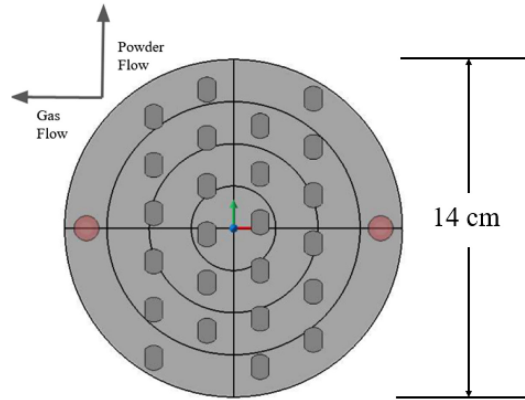
To assess the printing response of each blend, a design of experiments (DOE) concept was implemented. This commenced with a central composite design (CCD) with the intent of establishing the general effects of laser power, scan speed, hatch spacing, and the overarching VED on part density. The level values for this DOE, so-called DOE-1, are listed in Table 16. Ranges of 100-200W, 750-1250mm/s, and 0.05-0.15mm were selected based on values established in literature as well as previous experience with the AlSi10Mg alloy. Four specimens were built using the midpoint values for each parameter for the purpose of determining the degree of variance based on uncontrolled factors such as build plate position. The specific build parameters for 18 specimens are listed in Table 17. The build order was randomized to mitigate positional biases. Three builds were executed using this structure with AlN-C contents of 0%, 5%, and 10%.

Table 16: Parameters investigated in DOE-1

Factor	Level Values				
Laser Power (W)	100	120	150	180	200
Scan Speed (mm/s)	750	851	1000	1149	1250
Hatch Spacing (mm)	0.05	0.07	0.10	0.13	0.15

Table 17: Specific build parameters for DOE-1

Specimen	P (W)	v (mm/s)	d (mm)	VED (J/mm^3)
1	120	851	0.07	67.1
2	180	851	0.07	100.7
3	120	1149	0.07	49.7
4	180	1149	0.07	74.6
5	120	851	0.13	36.2
6	180	851	0.13	54.2
7	120	1149	0.13	26.8
8	180	1149	0.13	40.2
9	100	1000	0.10	33.3
10	200	1000	0.10	66.7
11	150	750	0.10	66.7
12	150	1250	0.10	40.0
13	150	1000	0.05	100.0
14	150	1000	0.15	33.3
15	150	1000	0.10	50.0
16	150	1000	0.10	50.0
17	150	1000	0.10	50.0
18	150	1000	0.10	50.0

Once a set of conditions that minimized porosity for the ceramic blends was established, a second general factorial DOE (so-called DOE-2) was run to more closely target optimal processing values for laser power and scan speed. Table 18 lists the level values for DOE-2. A range of laser powers from 180W-300W and scan speeds from 500-1250mm/s was selected based on the results of DOE-1. Each of the twelve parameter combinations

was duplicated, resulting in 24 cuboidal specimens of 0%AlN, 5%AlN-C, and 10%AlN-C. The parameters from DOE-2 were then reused to evaluate a 5%AlN-F chemical composition to study the effects of ceramic particulate size. This comparison was denoted as DOE-3. All density and hardness data derived from DOEs 1-3 were analyzed using MiniTab 19 statistical software.

Table 18: Parameters investigated in DOE-2 and DOE-3.

Factor	Levels	Level Values			
Laser Power (W)	3	180	240	300	
Scan Speed (mm/s)	4	500	750	1000	1250

Density measurements were completed per Archimedes principle, in accordance with ASTM B962, using oil infiltration. For each specimen, 4 hardness measurements were taken using the Rockwell E (HRE) scale (100kg load, ⅛" ball indenter) and averaged. Once the optimal parameter set was derived from DOEs 1-3, rectangular samples with dimensions 10 mm x 12mm x 75mm were fabricated and then machined into cylindrical tensile specimens (build plate configuration shown in Figure 25). Two groups of 0%AlN bars were fabricated: one was left as built (AB) and one was stress relieved (SR) at 285°C for 2 hours before air cooling. An additional group of 5%AlN-F specimens were built and subject to the SR cycle. Tensile tests were conducted using an Instron model 5594-200HVL 1MN load frame with a 50 kN load cell. Elongation was measured using an Epsilon 3542 extensometer. The specimens were loaded at a rate of 5MPa/s until fracture.
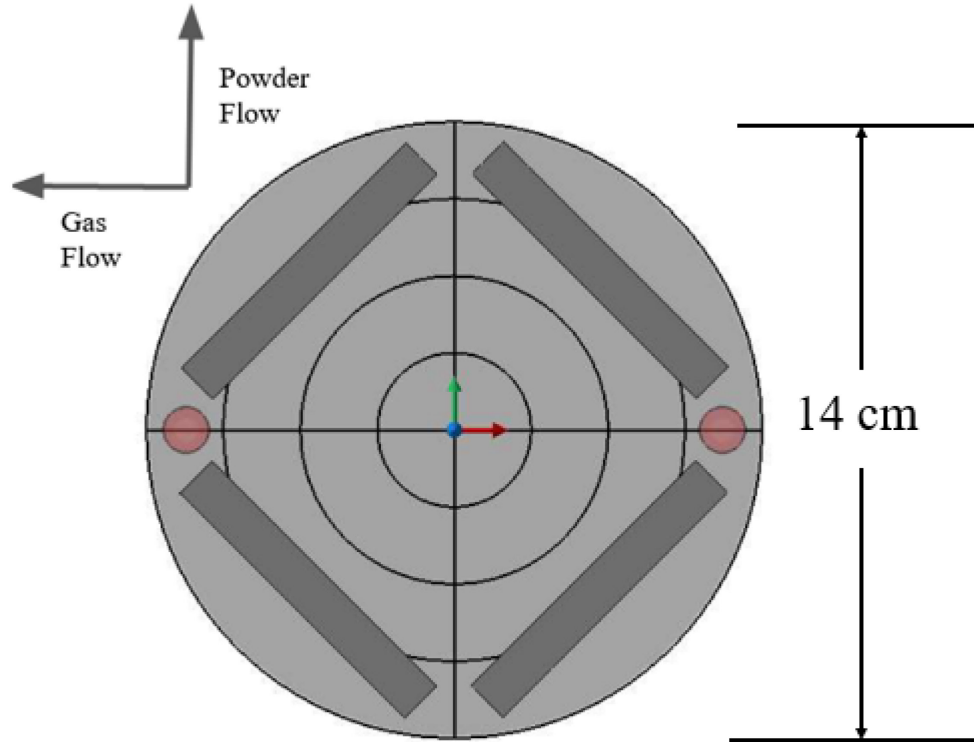
Figure 25: Build plate configuration used for tensile specimens.

Specimens for microscopy were sectioned in their respective planes using a diamond saw blade and mounted in a conductive Bakelite. All mounts were ground with a 240-grit silicon carbide paper on a Struers Tegramin 20 auto polisher, then polished using a series of abrasive suspensions. When required, etching was completed using Keller's reagent.

Optical images of all samples were taken using a Keyence VK-X1000 laser confocal microscope. SEM images of all powders, density cuboids, and tensile fracture surfaces were obtained using a Hitachi S-4700 SEM.

3.4 Results and Discussion

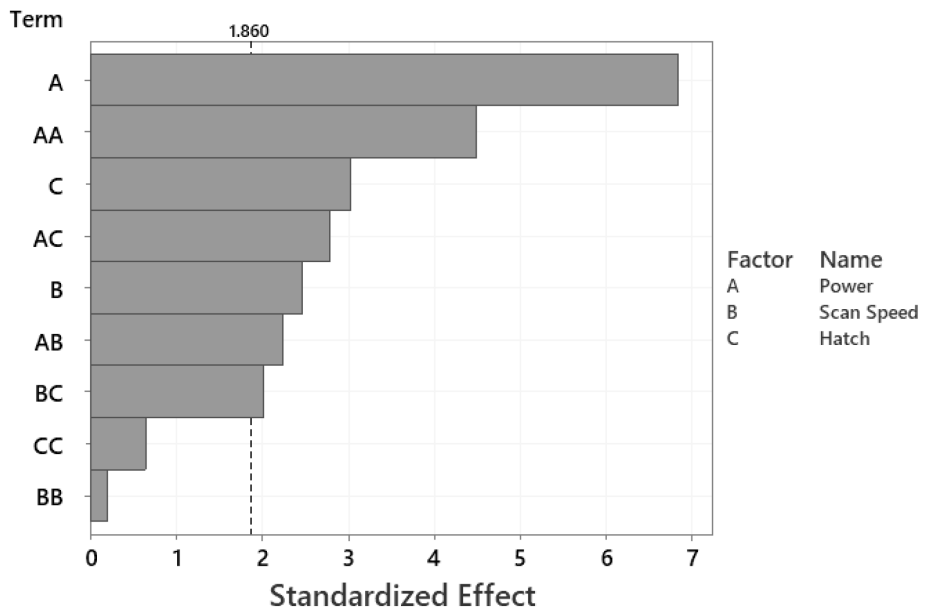### 3.4.1 General Effects of Process Variables (DOE-1)

An analysis of variance (ANOVA) was utilized to measure the standardized effects of key process parameters and their interaction effects as they pertain to density. A confidence interval of 90% ($\alpha = 0.1$) was selected to define significance. A measure of standardized effects for 0%AlN, 5%AlN-C, and 10%AlN-C blends are listed in Figure

26. Results show that over the range of parameters investigated, laser power had the most significant effect on part density. Singular effects of scan speed and hatch spacing were not significant to the density of the unmodified AlSi10Mg base powder but were significant with the two MMC powder blends, although significant interaction effects with power were observed. R-squared values for the analyses of the 3 builds were 89.5%, 92.6%, and 92.6%, respectively. Table 19 summarizes the P and F-values for this regression. Overall P-values of 0.005, 0.001, and 0.001 suggested that the regression model was suitably fitted to the data.
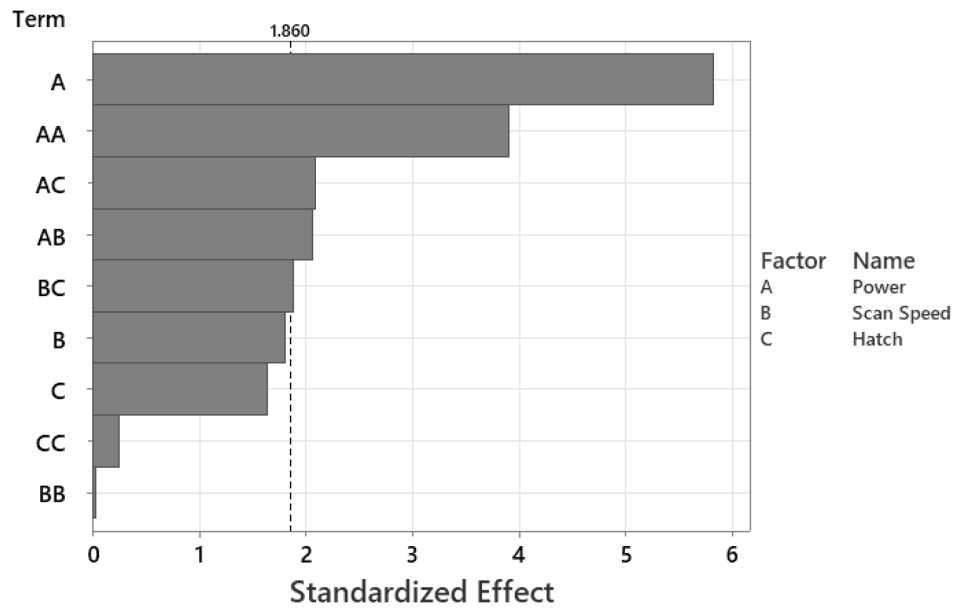
(a)

(b)
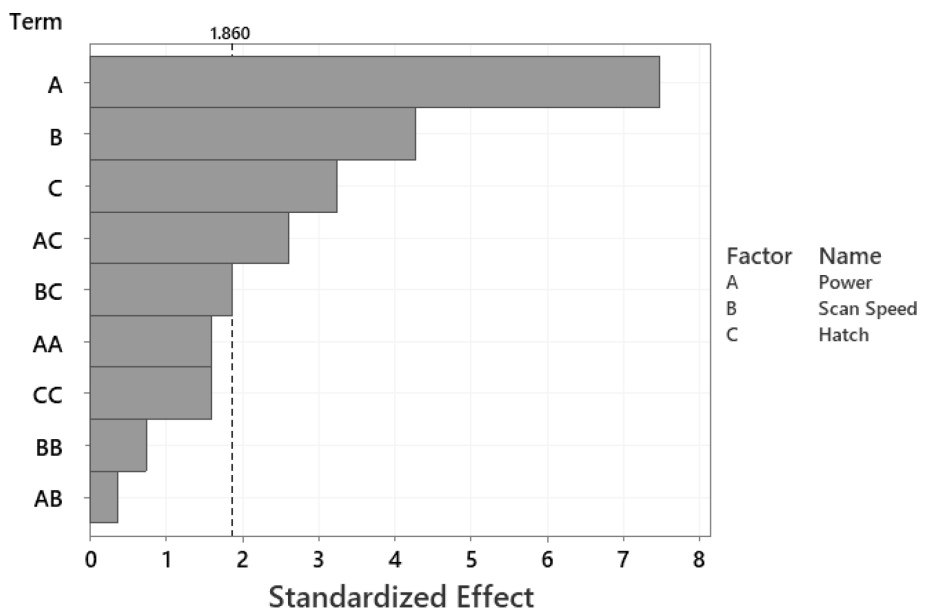
(c)

Figure 26: Standardized effects of process variables on density ($\alpha = 0.1$) for (a) 0%AlN, (b) 5%AlN-C, and (c) 10%AlN-C

Table 19: ANOVA table for density regression model developed for different powder systems.

Source	DoF	0%AlN		5%AlN-C		10%AlN-C	
		F	p	F	p	F	p
Model	9	7.57	0.005	11.06	0.001	11.22	0.001
Linear	3	13.29	0.002	20.64	0.000	28.17	0.000
P	1	33.91	0.000	46.65	0.000	55.80	0.000
v	1	3.28	0.108	6.10	0.039	18.19	0.003
d	1	2.69	0.139	9.18	0.016	10.51	0.012
Square	3	5.37	0.026	6.90	0.013	2.01	0.191
P*P	1	15.19	0.005	20.08	0.002	2.55	0.149
v*v	1	0.00	0.980	0.04	0.850	0.56	0.478
d*d	1	0.07	0.805	0.41	0.538	2.54	0.150
Interaction	3	4.06	0.050	5.63	0.023	3.48	0.070
P*v	1	4.23	0.074	5.04	0.055	0.14	0.718
P*d	1	4.39	0.069	7.80	0.023	6.79	0.031
v*d	1	3.55	0.096	4.07	0.079	3.51	0.098
Error	8						
Lack-of-Fit	5	35.12	0.007	330.98	0.000	1.02	0.527
Pure Error	3						
Total	17						

In the context of optimization, laser power, scan speed, and hatch spacing were varied while layer thickness was held constant. These factors contribute to the volumetric energy density (VED), which is given by Equation 1 [98]:

$$VED = \frac{P}{vhd}$$

Where P represents the laser power, v is the scan speed, h is layer height, and d is the inter-track, or hatch, spacing. As the overall energy input is dependent on power, scan speed, and hatch spacing, interaction effects between the variables are expected.

The specimens associated with the two lowest VED values (26.8 and 33.3J/mm^3), were unable to be printed due to insufficient powder melting. Figure 27 shows a series of contour maps generated from the response surface regression. Green areas identify parameter sets where relatively high density is expected, while blue areas are associated with poor densification. Each map illustrates the effects of two parameters for a prescribed chemistry while the third (that was held constant) is shown on the lefthand side. Laser power exhibited the most significant contribution to part density. At laser powers below 150W, densification was only possible at the lowest scan speed and hatch spacing of those tested. Although 0%AlN and 5%AlN-C demonstrated sizable regions over which a relatively high density could be expected, the 10%AlN-C matrix composite was far less robust as it exhibited poor densification across all parameter sets, with a maximum density of 96% realized. However, the contour maps for this system showed a region of high expected density as laser power approached 200W. The sole specimen built at P = 200W, exhibited the highest density for all three chemistries. Due to the observed benefits of increasing laser power, the range of laser powers considered was increased for DOE-2.
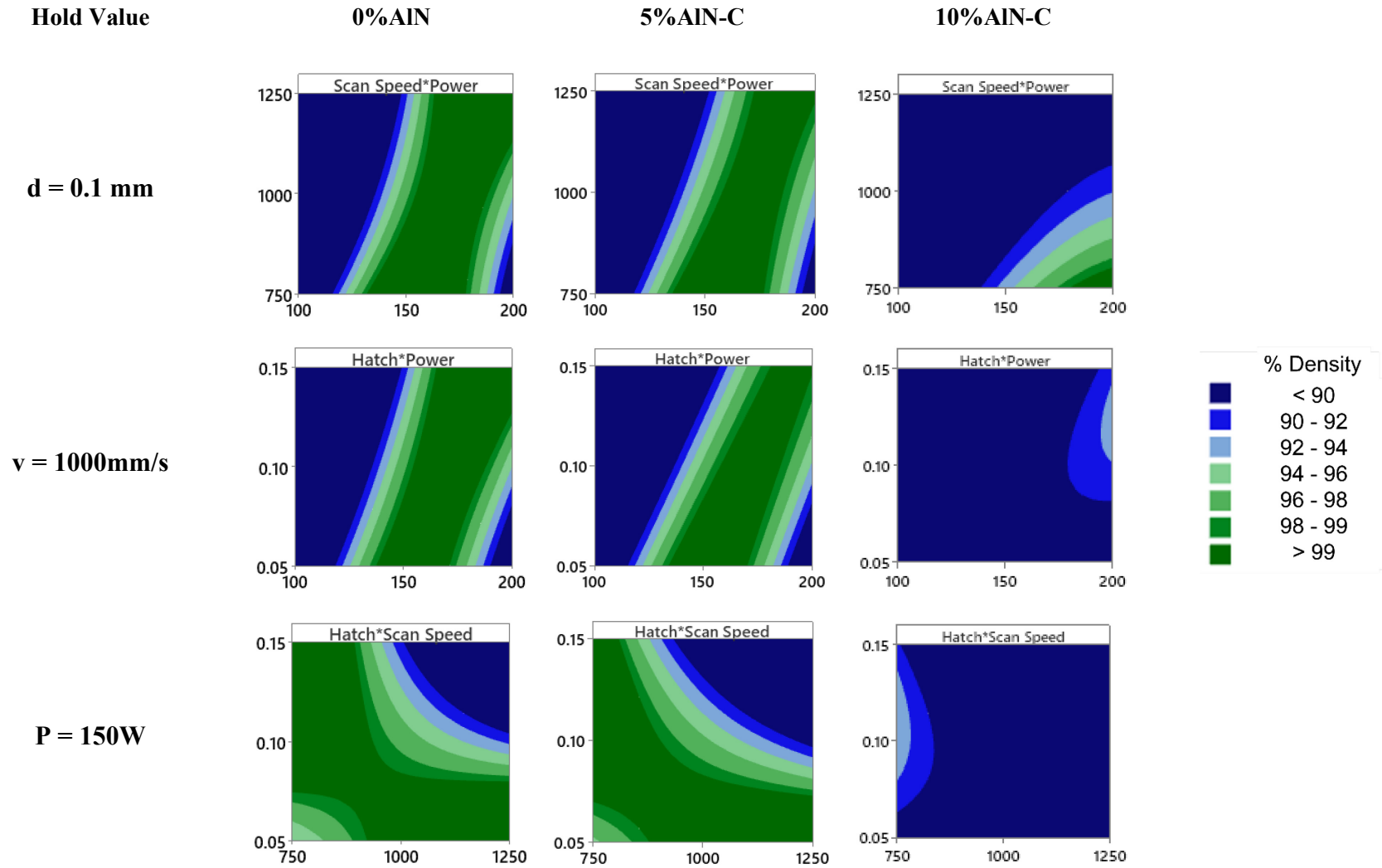
Figure 27: Contour maps for density data deduced from DOE-1

Images of each powder chemistry at the centre point conditions (P= 150W, v = 1000mm/s, d =0.10mm) employed in DOE-1 appear in Figure 28. Notably, the extent of porosity increases substantially as AlN content increases. Irregular lack of fusion (LOF) porosity was the primary defect structure observed in these specimens. LOF porosity occurs when insufficient melting prevents bonding between adjacent melt pool tracks. Due to the propensity of aluminum alloys to oxidize and the elevated melting points of these oxides, insufficient laser power leads to areas of unmelted powder and thus gaps between layers, such as the pore seen in Figure 29. The irregular morphology of these pores renders them more detrimental to a component under load than a spherical pore as they have more surface area to act as a stress concentration point.

Thermodynamically stable surface oxide films, which are inherent to aluminum, have an inhibitive effect on bonding between layers as they prevent wettability between the liquid melt pool and solid previous layer [99]. These films become more prevalent in powder-based processes such as AM due to the higher surface area of powders compared to wrought counterparts [100]. The introduction of fine, irregularly shaped ceramic particles contributes to the overall surface area of the powder bed. While aluminum nitride is known to be wetted by molten aluminum [34], insufficient breakdown of the oxide film and the presence of adsorbed gases on the AlN surface may act as contributors to the increase in LOF porosity as the ceramic content is increased.

In the etched state, the distinct shape of the overlapping melt pool boundaries was observed. Distinct microstructural regions indicate the thermal history. At the boundary, the microstructure was coarsened due to the proximity of the region to the subsequent layer, becoming a heat affected zone as the next laser scan traversed. As the distance from the melt pool boundary increased towards the core of the melt pools, a finer microstructure was then observed. Acceptable defect density is observed in the 0%AlN specimen, as only small pores < 20 μm in diameter were present. In the 5%AlN-C composite, LOF defects accumulate at these boundaries which are the joining location between the molten metal and previously solidified layer. In the 10% AlN-C composite, LOF defects span distances equivalent to multiple layers. In both composites, the ceramic

particulate appears to be effectively distributed with no significant evidence of agglomeration.
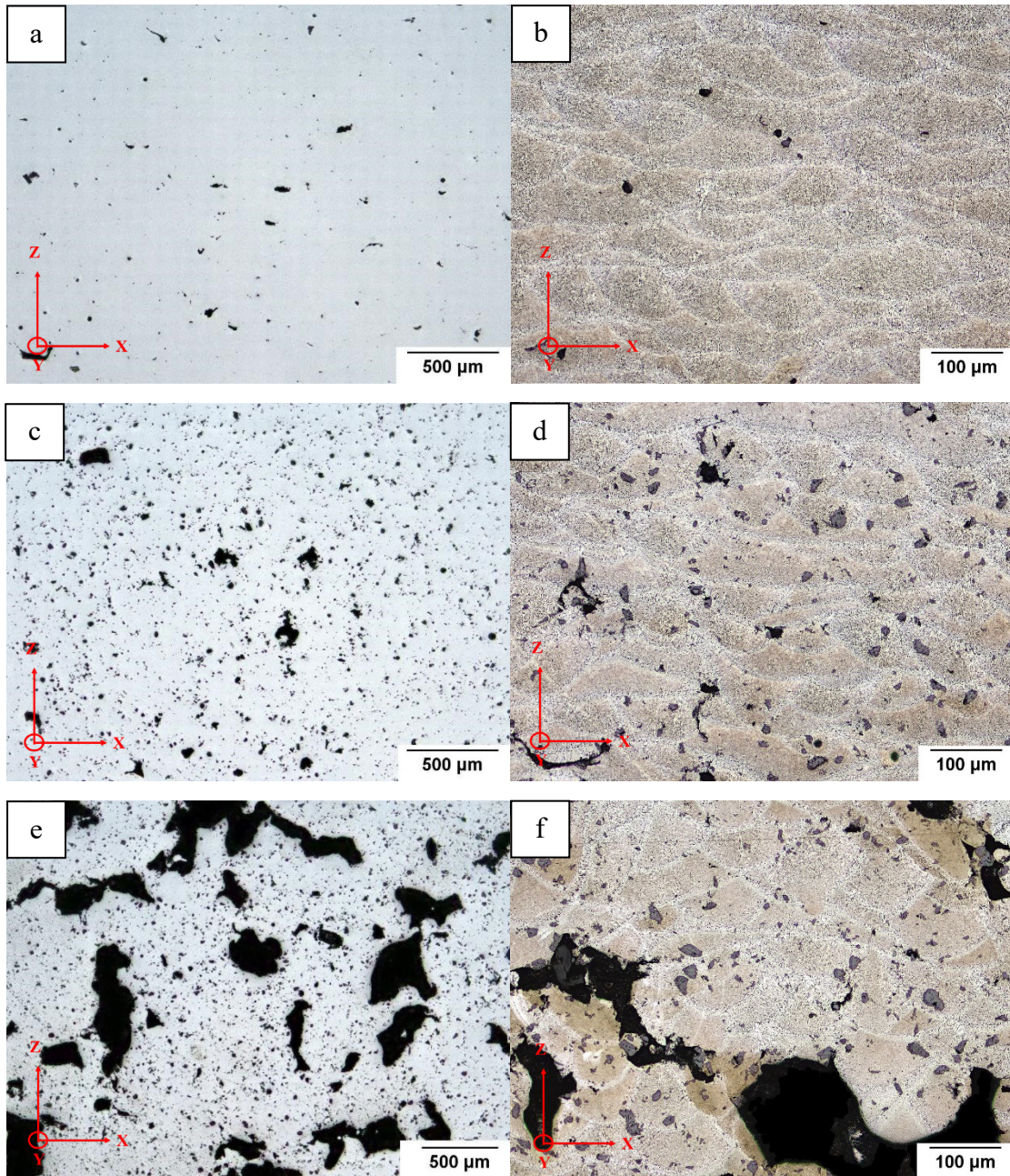

Figure 28: Optical micrographs at 5x and 20x magnification (etched with Keller's reagent) for (a),(b) 0%AlN (98.9% dense), (c),(d) 5%AlN-C (96.9% dense), and (e),(f) 10%AlN-C (84.3% dense) at the centre point conditions (150W, 1000mm/s, 0.10mm) employed in DOE-1.
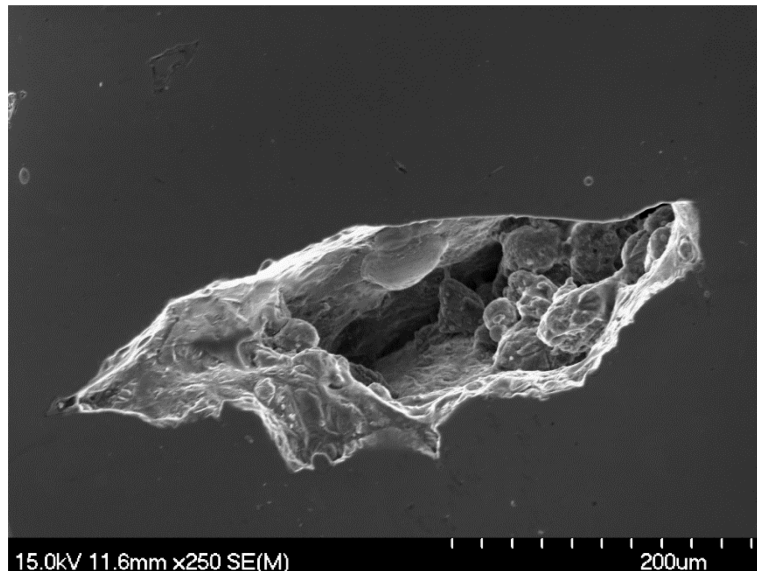
Figure 29: LOF pore in 0%AlN specimen

3.4.2 Refined Assessment of Process Parameters (DOE-2)

A wide range of VED values (48-200 J/mm^3) was utilized in this experiment to try and ensure that the extremes of insufficient fusion and keyhole melting were captured. Density versus VED curves for the three blends are shown in Figure 30 along with a polynomial regression fitted to each data set. Since %AlN was treated as a discrete value while laser power and scan speeds were treated as continuous variables, regression analyses were conducted for each blend chemistry separately. Optimal VED for the three material systems ranged between 60-80J/mm^3, comparable to literature values outlined previously. At a VED of 80J/mm^3, multiple specimens demonstrated a noticeable difference in density given that the same VED was achieved using different combinations of laser power and scan speed. This demonstrates that while the correlation between VED and density may be fitted, optimization of the underlying power and scan speed can improve density further.
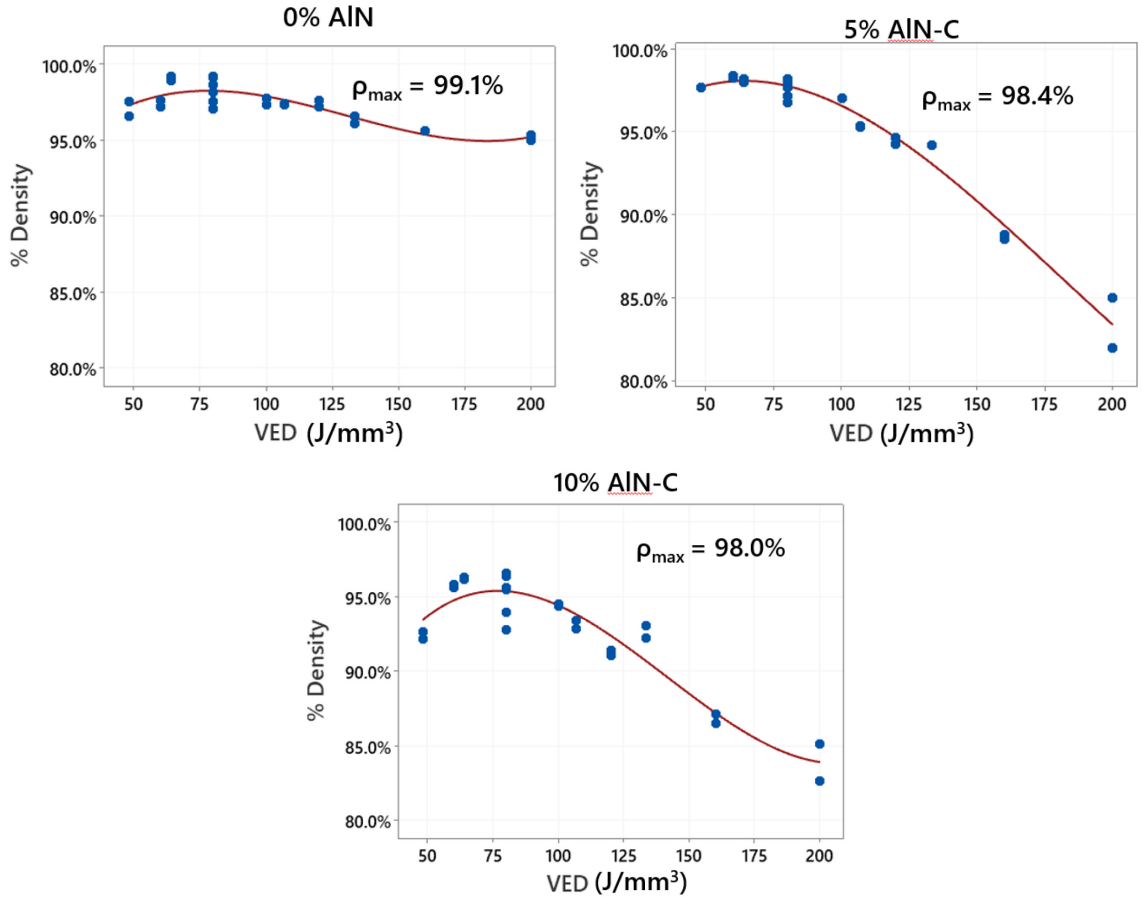
Figure 30: Density versus VED curves for each powder blend assessed in DOE-2.

At the extremes (48 and 200J/mm^3) for the base AlSi10Mg alloy, specimen density and hardness were comparatively poor, although noticeably lowest in the high VED case. Addition of 5% AlN contributed to lower density at the upper VED limit and comparable density at the lower limit. Addition of 10% AlN resulted in lower density at both lower and higher VED. Overall, the lowest porosity was observed in specimens with inputs of 240W, 1000mm/s and 240W, 1250 mm/s. The maximum density of the 0%AlN, 5%AlN-C, and 10%AlN-C materials were 99.1%, 98.2%, and 97.9% of theoretical density, respectively showing a decrease in density with increasing AlN addition.

Figure 31 shows the contour maps for hardness and density for the three chemistries examined in DOE-2. The expected correlation between density and hardness was observed. Additionally, these maps showed a discrepancy in the ideal processing parameters between the base alloy and the composites. With AlN addition, decreases in laser power and scan speed improved densification. In terms of hardness, the predicted region of HRE > 90 increased with increasing AlN addition, despite an accompanying drop in density as AlN content increased, demonstrating a strengthening effect. Both density and hardness were favoured in the MMCs as laser power approached 180W and scan speed approached 1000mm/s.

High laser absorptivity of AlN [101] accompanied with lower thermal diffusivity of the metal-ceramic blends appears to reduce the power requirement necessary for melting; an effect that has been demonstrated for AlSi10Mg-SiC and AlSi10Mg-TiB$_2$ AMCs [92] as well. Another possible contribution is the promotion of increased laser reflections within the powder bed due to the relatively high surface roughness of the ceramic additive [102].
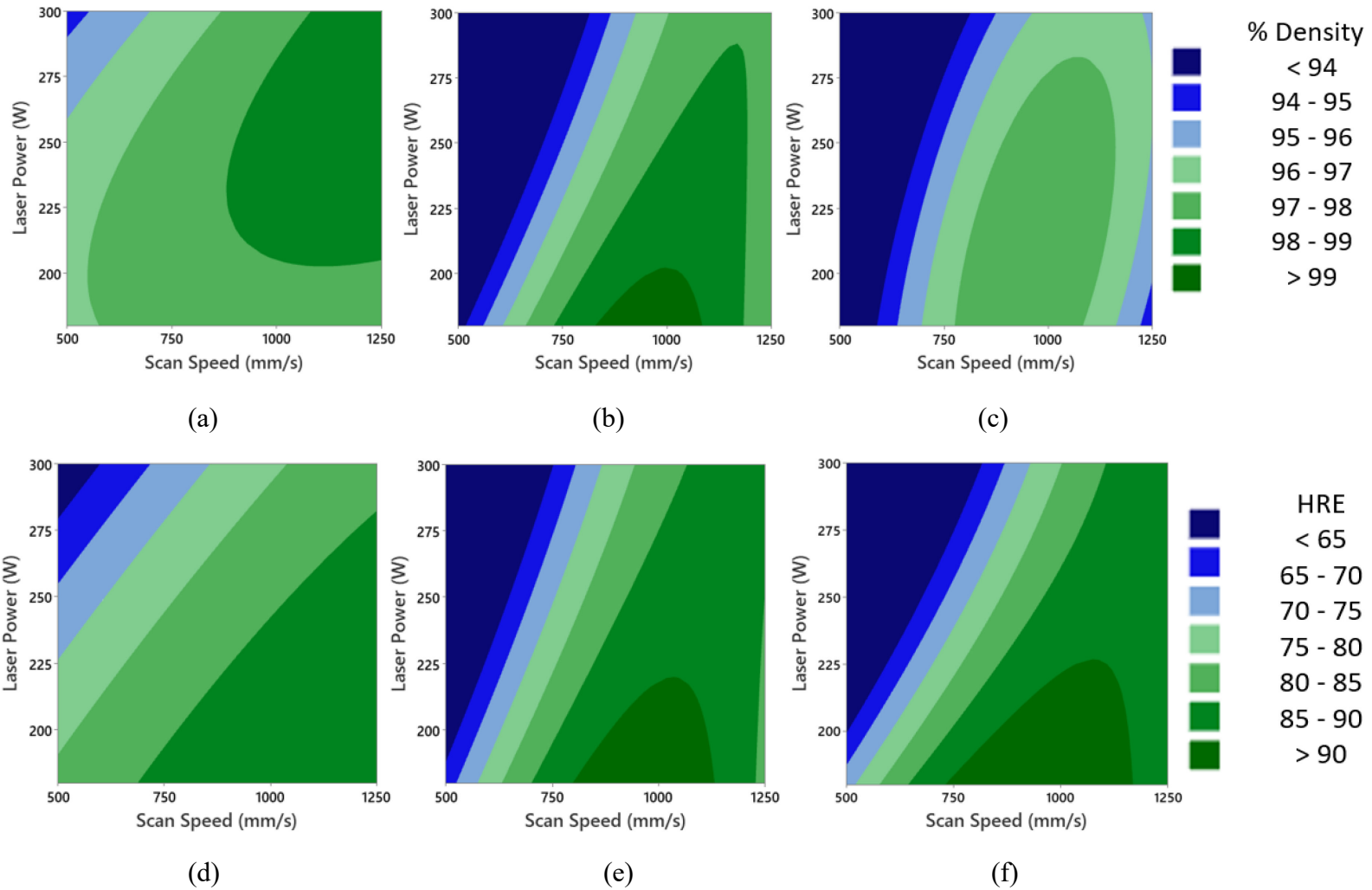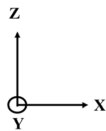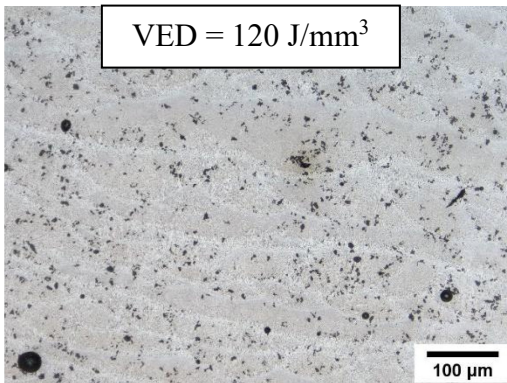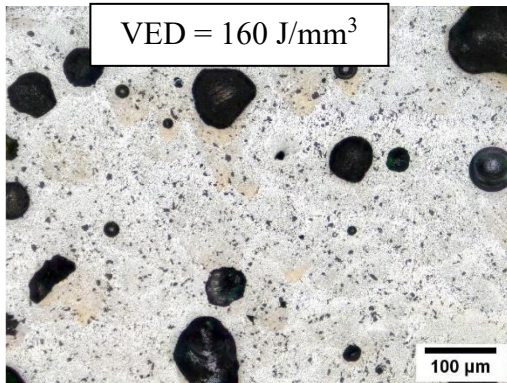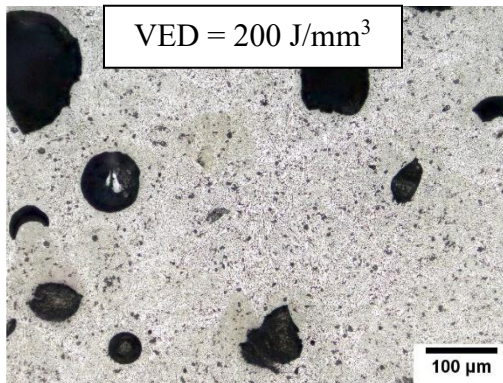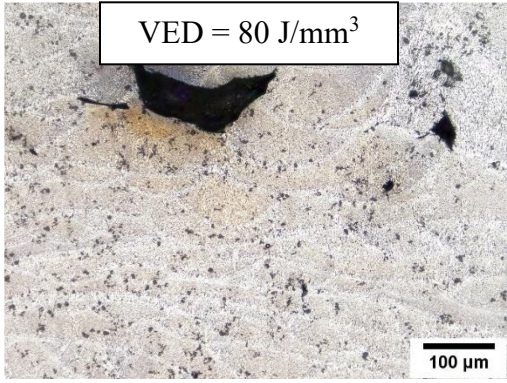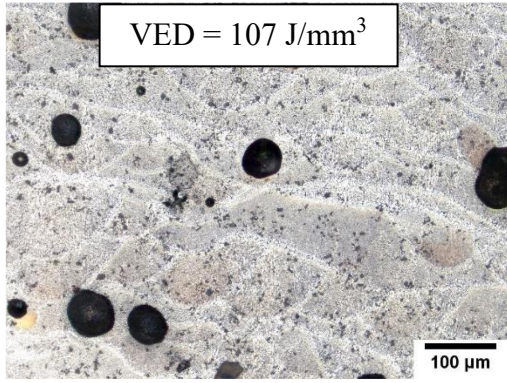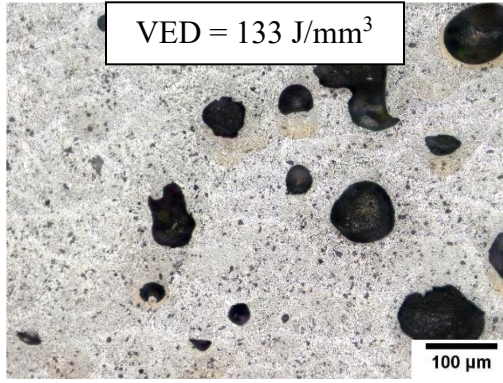
Figure 31: Contour maps for density and HRE for 0%AlN (a, d), 5% AlN-C (b, e), and 10%AlN-C (c, f) as functions of laser power (W) and scan speed (mm/s), derived from DOE-2
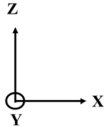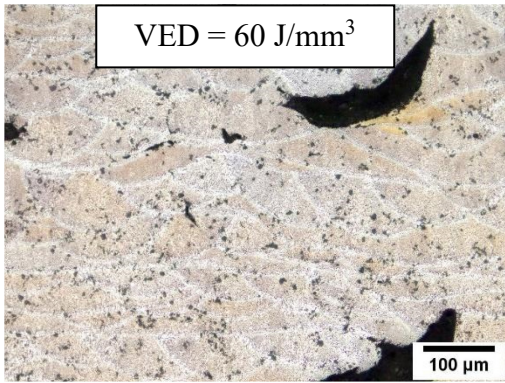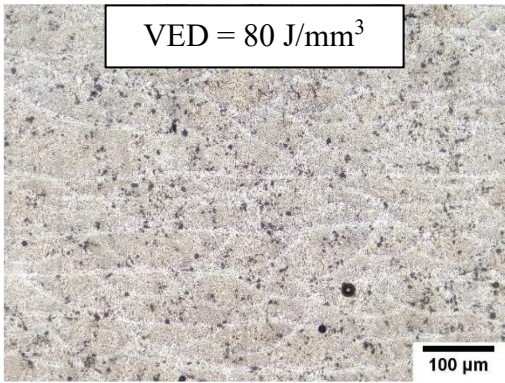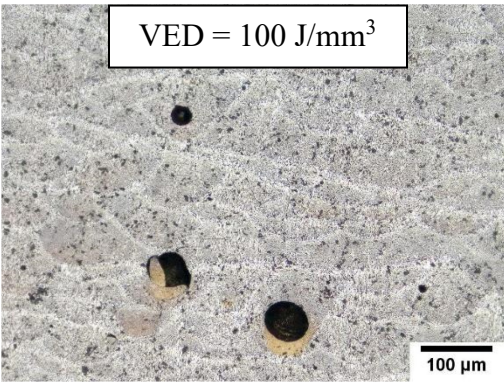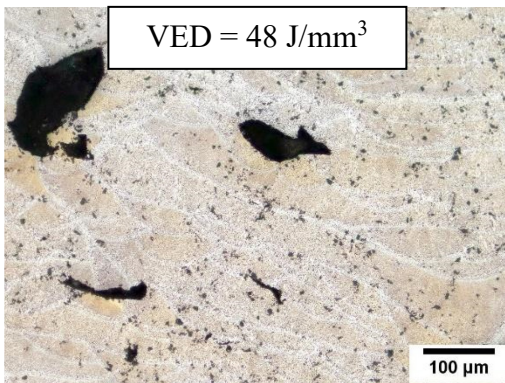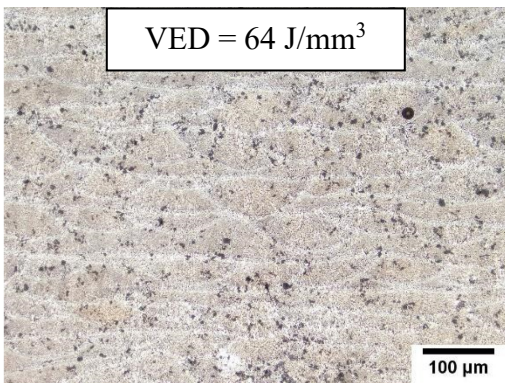
3.4.3 Effect of Ceramic Particulate Size (DOE-3)

A build using a formulation of AlSi10Mg and 5%AlN-F was then conducted per the same power and scan speed levels established in DOE-2. The microstructure of a specimen subjected to each parameter set is shown in Table 20. LOF porosity was observed at the lowest volumetric energy density (48-60J/mm^3) while extensive keyholing was associated with the high energy density (100-200J/mm^3) range. When VED was in the range of 80 J/mm^3, the AMC product was near full density. Micrographs of these highest density specimens exhibited only infrequent spherical gas pores. Gas porosity in aluminum AM is often caused by the dissolution and entrapment of surface oxides in the melt pool [103]. The thermodynamic stability of the aluminum oxide phase makes elimination of this effect unfeasible [104], but favourable compared to insufficient fusion between layers, as spherical pores are less detrimental to mechanical strength than those that are irregularly shaped [21]. It is notable that the Archimedes density measurements on specimen fabricated at 80 J/mm^3 revealed values of 99.1% and 98.9% of full theoretical. Past experience has shown that this technique generally yields a relatively conservative assessment of specimen density. As such, the true density is likely high in keeping with the micrographs which demonstrate a very low concentration of residual porosity.

Qualitatively, the AlN appeared to be well-distributed in the matrix. This was viewed as a positive trait given that this can maximize stress distribution under load yet it can be a significant hurdle with fine ceramic additives, especially at higher scan speeds [94]. When wettability of the molten metal to the ceramic interface is poor, rejection of the ceramic to the melt pool boundaries can occur due to Marangoni convection forces [105]. Thus, successful particle rearrangement is suggestive of good wetting between the molten aluminum and AlN across the investigated parameter set.

Table 20: Micrographs of 5%AlN-F specimens built in DOE-3.

$\begin{smallmatrix} Z \\ \uparrow \\ \circ \rightarrow X \\ Y \end{smallmatrix}$	180W	240W	300W
500mm/s	VED = 120 J/mm^3 100 μm	VED = 160 J/mm^3 100 μm	VED = 200 J/mm^3 100 μm
750mm/s	VED = 80 J/mm^3 100 μm	VED = 107 J/mm^3 100 μm	VED = 133 J/mm^3 100 μm

	180W	240W	300W
1000mm/s	VED = 60 J/mm^3	VED = 80 J/mm^3	VED = 100 J/mm^3
1250mm/s	VED = 48 J/mm^3	VED = 64 J/mm^3	VED = 80 J/mm^3

To evaluate the matrix-particulate interface, EDS mapping was conducted. Figure 32 shows that, chemically, the ceramic and matrix areas remained distinct. This implied that the ceramic remained solid while the matrix melted and solidified around it as the laser was rastered over the powder bed. Additionally, EDS mapping identifies the presence of a silicon rich fibrous network; this network serves a similar load bearing purpose to the ceramic additive in limiting dislocation movement under load [106].
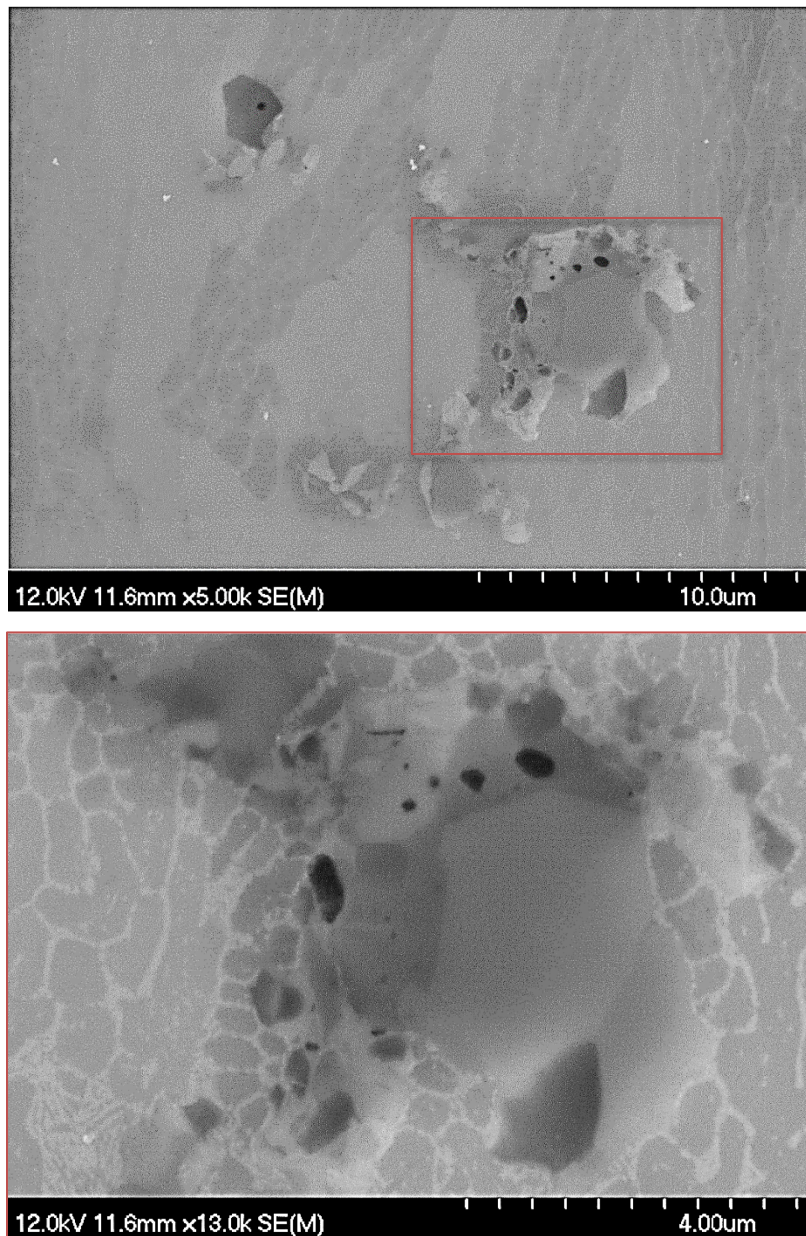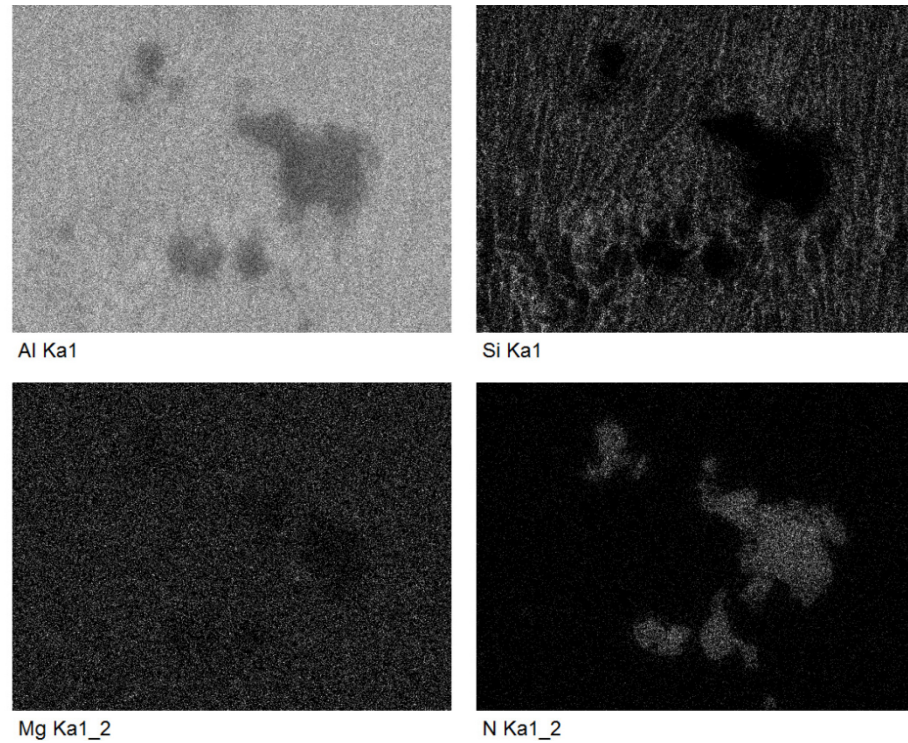
Figure 32: SEM images and accompanying EDS maps of a 5%AlN-F specimen.

To examine the effect of ceramic particle size on component density and hardness, results from the 5%AlN-F specimens were compared to the 0%AlN and 5%AlN-C specimens from DOE-2. Figure 33 shows the relation between density and hardness as a function of VED for the 0%AlN, 5%AlN-C, and 5%AlN-F materials as determined by a fitted regression model. Despite lower density, hardness of the two MMCs remained higher in the established optimal range of 60-80J/mm^3; residual porosity in this range was not as detrimental to the hardness as the ceramic additive was beneficial. Differences between the fine and coarse ceramic additive were not substantial.
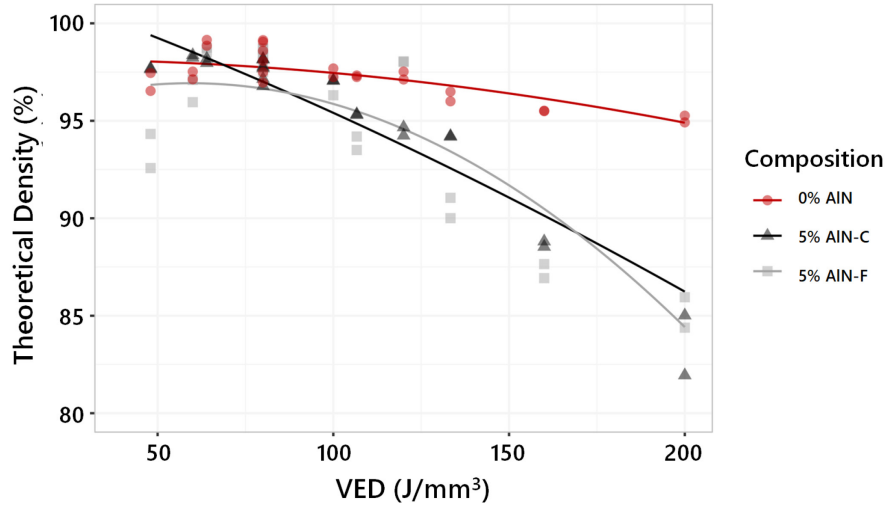
(a)
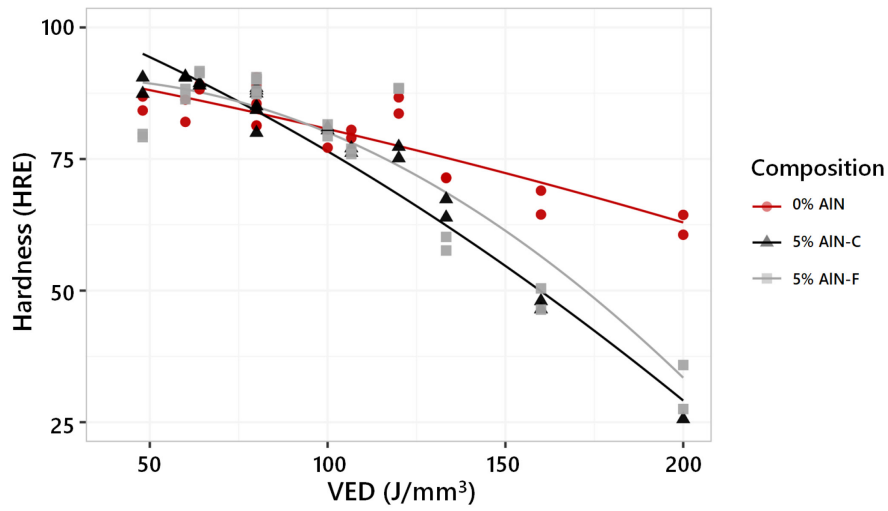
(b)

Figure 33: Density (a) and hardness (b) results from DOEs 2-3.

Owing to improved density, higher hardness, and improved flowability (Table 15), the 5%AlN-F formulation was selected for comparison with the 0%AlN base alloy for tensile testing. As the maximum hardness and density for both formulations were achieved with P = 240W and v = 1000mm/s, these parameters were selected for tensile builds.

3.4.4 Tensile Testing

Tensile bars, as well as cuboidal specimens for microstructural examination, were printed using the optimized parameters from DOE-2 and DOE-3 (240W, 1000mm/s). Physical and mechanical properties of these specimens in the as-built and stress-relieved conditions are listed in Table 21. Notably, densities of the tensile bars were observed to be marginally lower than the cuboids produced in DOEs 2 and 3. As these bars were larger than the cuboids, longer laser exposure times were required which led to significant spatter, increasing the roughness of the previous layer upon coating. This coupled with a very different heat flow was believed to be responsible for the observed density differences.

Results showed a beneficial response to the stress-relief cycle (285°C for 2 hours). A 172% increase in ductility was observed in the 0%AlN specimens, while UTS and YS decreased by 6% and 17%, respectively. In comparison, the 5%AlN-F composite exhibited similar YS and UTS to the 0%AlN specimen despite having a measurably lower density of 97.1% as compared to 98.6% for the AlN-free counterpart. Figure 34 shows the stress-strain relation for the three sets of specimens tested.

It is important to note that mechanical properties were measured orthogonal to the build direction, and mechanical anisotropy is possible due to potential epitaxial grain growth in the build direction as layers are added. A common consequence of LPBF processing is the re-melting of previously deposited layers, and the high thermal gradients and cooling rates can cause epitaxial growth which may span multiple layers [107]. Substantial differences in ductility have been observed in LPBF-processed AlSi10Mg between the XY and Z directions because of this phenomenon [108]. Further investigation will be required to determine the effects of ceramic addition and stress relief on these properties in the build direction.

Table 21: Tensile testing results

Specimen ID	Condition	ρ (%)	E (GPa)	UTS (MPa)	YS (MPa)	ε_{max} (%)
0%AlN	AB	98.1 ± 0.7	63 ± 4	300 ± 22	208 ± 5	2.9 ± 1.0
0% AlN	SR	98.6 ± 0.6	58 ± 3	281 ± 5	173 ± 2	7.9 ± 0.9
5%AlN-F	SR	97.1 ± 1.0	64 ± 3	278 ± 7	177 ± 2	5.9 ± 1.2
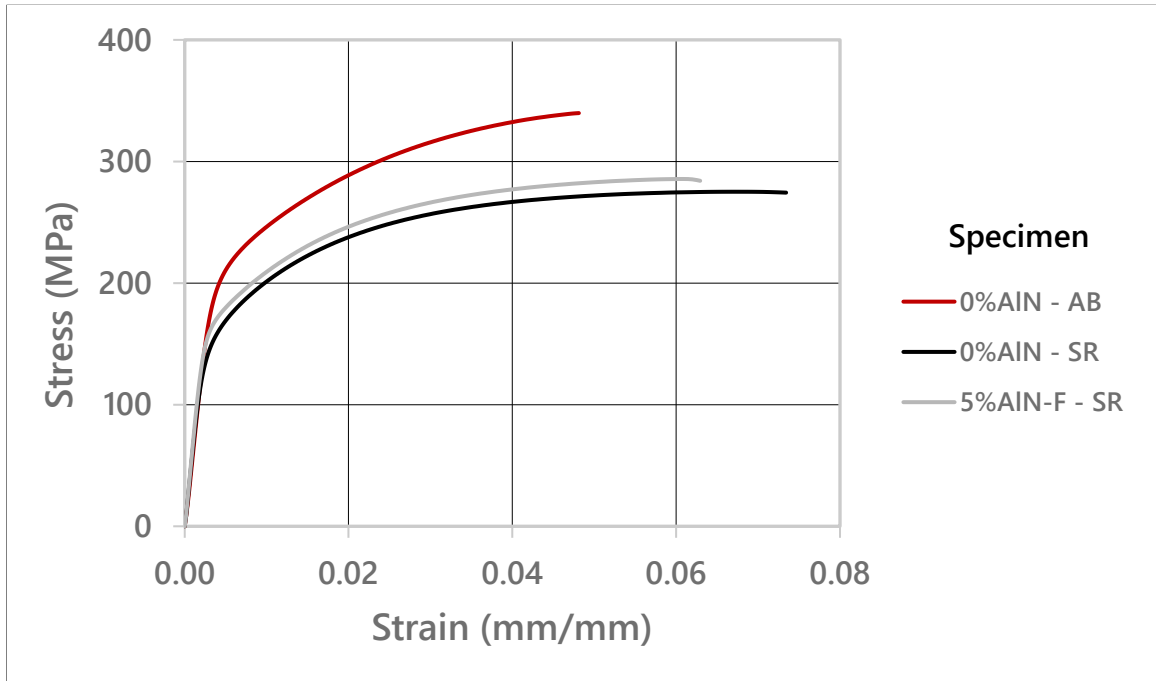
Figure 34: Stress-strain curves for "best case" tensile specimens

AM processes such as LPBF can impart thermally induced residual stresses in materials. These residual stresses can be mitigated by holding the build plate at elevated temperatures to reduce thermal gradients and thus residual stresses [24]. With a build plate temperature >200°C, residual stresses in LPBF-manufactured AlSi10Mg have been reduced to negligible levels [109]. Thus, since all tensile specimens were built with a build plate temperature of 220°C, the improvement in ductility is expected to be driven by microstructural changes rather than from relief of thermally induced stresses.

Figure 35 shows the microstructure of the as-built and stress relieved 0%AlN and 5%AlN-F in closer detail. Here, notable differences in the microstructure were

70

manifested through application of the post-build stress relief. One pertained to the eutectic network of silicon particles. In the as-built condition, the fibrous silicon network is fine and primarily connected. As a result of the stress relief cycle, the morphology of this network coarsened and connectivity was decreased. This silicon network has a known load bearing effect [106], and the globularization of silicon and eventual breakdown of this region is the expected cause of the reduced tensile strength and increased ductility post-build heat treatment. Additionally, Si precipitates are observed to form within the α-Al matrix. Compared to the 0%AlN specimen, the addition of 5%AlN-F does not appear to disrupt this network and appears to be completely distinct from the underlying microstructure. The interface between the AlN particulates pictured in images e-h is devoid of any cracking.

Another observable difference between the as-built and stress-relieved conditions of both 0%AlN and 5%AlN-F specimens is the introduction of submicron dark regions. The reintroduction of voids has been observed in AlSi10Mg AM following T6 heat treatment [110] although the stress relief temperature is lower in this case. Porosity can be relieved using a hot isostatic press (HIP), but these pores are comparatively small and not expected to be detrimental due to their small size relative to pores introduced in the AM process.
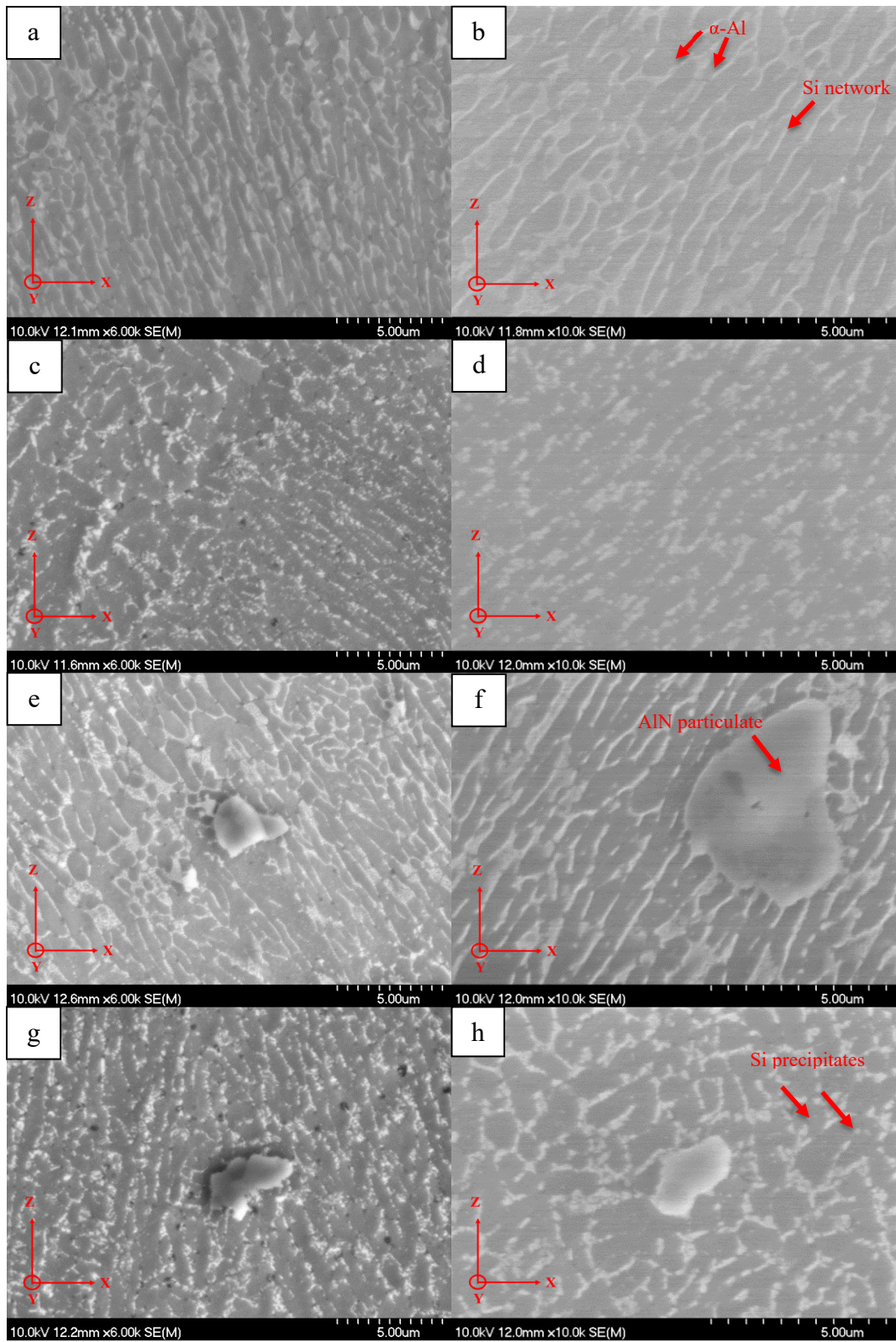
Figure 35: Microstructure of (a) AB 0%AlN, (b) SR 0%AlN, (c) AB 5%AlN-F, (d) SR 5% AlN-F.

3.5 Conclusions

Through completion of the work detailed in this study, the following conclusions have been reached:

- DOE-1 showed that, under the parameters investigated, laser power was the most significant variable in terms of specimen density. Poor consolidation was observed with laser powers below 150W regardless of the total VED employed.
- The prevalence of irregular LOF pores increased in both quantity and size outside of the optimal VED range in DOE-1.
- From DOE-2, the optimal range of VED was determined to be 60-80 J/mm^3 for all chemistries, although increased laser absorptivity in the MMCs suggested a lower power and scan speed while remaining in this VED range could prove beneficial.
- In DOE-3, 5%AlN-F specimens were successfully built with $\rho > 98.5\%$
- Comparing the 0%AlN and 5%AlN-F specimens built using the optimized parameters (P=240W, v=1000mm/s, d=0.10mm), an increase in gas porosity was observed in the MMC specimens. The cause of this is believed to be the lower thermal diffusivity in the MMC powder bed, leading to higher localized temperatures and thus increased vaporization.
- Tensile testing showed a positive response in elongation in the AlSi10Mg alloy following a stress-relief heat treatment, at the expense of YS and UTS.
- Despite lower density, the stress-relieved MMC demonstrated YS and UTS comparable to the stress-relieved AlSi10Mg.
- Both 0%AlN and 5%AlN-F chemistries exhibited the same microstructural response to heat treatment in the globularization of the Si rich phase

3.6 Acknowledgements

4. SUMMARY AND CONCLUSIONS

The objective of this work is to examine the performance of admixed aluminum nitride as an additive to AlSi10Mg and its effect on the processability of this alloy using laser powder bed fusion. Due to scarcity of work specific to this AMC system in open literature, this study serves as a preliminary parametric analysis to be built upon.

4.1 Physical Powder Characteristics

One of the challenges to aluminum LPBF is overcoming poor powder flowability. Introducing a ceramic additive to the feedstock exacerbates this challenge due to the mismatch in powder morphology. Although the 5%AlN-F blend proved to have improved powder flowability in preliminary testing over the 5%AlN-C blend, spreadability of the MMC blends was observed to be poorer than the AlSi10Mg powder on its own.

4.2 Effects of Process Variables

A design of experiments (DOE) approach was strategically used to measure the effects of multiple LPBF processing parameters (laser power, scan speed, and hatch spacing) on the consolidation of AlSi10Mg and to identify any variations in these requirements as a result of the AlN additive. Across the parameter set, a minimum laser power of 150W was required to successfully consolidate components for all chemistries examined. An ideal processing window of 60-80J/mm3 was determined using a polynomial regression fit to the density results of all chemistries tested.

There were two notable responses from the AMC builds that differed from 0%AlN. Firstly, the increase in porosity outside of the optimized processing window was more prevalent as AlN content increased. This observation held true for both the high VED (keyhole melting) and low VED (insufficient fusion) cases. Secondly, a shift in the processing window towards lower powers and scan speeds was observed. At these parameters, LOF porosity which was observed in the 0%AlN specimens was eliminated. Although the resulting density was comparable due to other sources of porosity such as gas pores, LOF porosity was successfully eliminated with lower power requirements,

owing to the higher absorptivity of AlN and the lower thermal diffusivity of the MMC blends.

4.3 Matrix-Ceramic Interface

The most desirable mechanical properties of AMCs require excellent bonding between the ceramic particulate and aluminum alloy matrix. EDS mapping showed the expected chemical stability of the AlN throughout the melting process, indicating that melt pool temperatures were low enough to prevent melting of the ceramic. The good dispersion of ceramic within the microstructure, as confirmed by optical microscopy, indicates a good wetting response between molten aluminum and AlN, as particulates were not rejected by the solidifying front. This is a typical challenge with *ex situ* MMC fabrication methods, which tend to be less complex than forming ceramics as a reaction product *in situ*.

However, ceramic addition did not successfully translate to improved mechanical properties. This may be a function of low density in the 5%AlN-F tensile bars compared to both the 0%AlN counterpart and previous density cuboids subjected to the same conditions. Reducing laser power and scan speed may be necessary for larger components such as tensile bars as the spatter associated with higher power can contribute to an uneven surface, as well as inconsistency in part density based on build location.

4.4 Future Work

As this research was the beginning of the group's research into AMCs manufactured using AM technologies, there is potential for continued studies.

1. Further optimization to assess the build response to other parameters such as layer height, scan strategy, and build plate temperature
2. Due to time and material constraints, mechanical properties of the base alloy and AMCs were only measured perpendicular to the build direction. These properties should also be measured parallel to the build direction, as mechanical anisotropy

can be problematic in aluminum AM due to columnar grain growth that may span multiple layers.

3. Electron back scatter diffraction (EBSD) can be utilized to determine the aluminum nitride's functionality as a grain refiner.

4. An examination of the 5%AlN-F fracture surface to determine the failure mechanism for this specimen

5. Tribological assessment of the 5%AlN-F composite, specifically to measure wear resistance, should be pursued.

REFERENCES

[1] E. Toyserkani, D. Sarker, O. O. Ibhadode, F. Liravi, P. Russo, and K. Taherkhani, *Metal Additive Manufacturing*. John Wiley & Sons, 2021.

[2] T. DebRoy *et al.*, "Additive manufacturing of metallic components – Process, structure and properties," *Prog. Mater Sci.*, vol. 92, pp. 112–224, Mar. 2018.

[3] S. Chowdhury *et al.*, "Laser powder bed fusion: a state-of-the-art review of the technology, materials, properties & defects, and numerical modelling," *Journal of Materials Research and Technology*, vol. 20, pp. 2109–2172, Sep. 2022.

[4] J. H. Martin, B. D. Yahata, J. M. Hundley, J. A. Mayer, T. A. Schaedler, and T. M. Pollock, "3D printing of high-strength aluminium alloys," *Nature*, vol. 549, no. 7672, pp. 365–369, Sep. 2017.

[5] Y. Ding, J. A. Muñiz-Lerma, M. Trask, S. Chou, A. Walker, and M. Brochu, "Microstructure and mechanical property considerations in additive manufacturing of aluminum alloys," *MRS Bull.*, vol. 41, no. 10, pp. 745–751, Oct. 2016.

[6] "Metal additive manufacturing in aerospace: A review," *Mater. Des.*, vol. 209, p. 110008, Nov. 2021.

[7] EOS, "3D Printing for Serially Produced Vehicles." https://www.eos.info/en/all-3d-printing-applications/mobility-logistics/automotive-industry-3d-printing/serially-produced-vehicles (accessed Oct. 16, 2022).

[8] J. D. M. Council, "Department of Defense additive manufacturing strategy," *Deputy Director for Strategic Technology Protection and Exploitation, Office of the Under Secretary of Defense for Research and Engineering*, 2021, [Online]. Available: https://www.3dpulse.ru/files/nodus_items/0010/5320/attaches/dod-additive-manufacturing-strategy.pdf

[9] "About Us - HI-AM." https://nserc-hi-am.ca/about-us/ (accessed Oct. 20, 2020).

[10] E. O. Olakanmi, R. F. Cochrane, and K. W. Dalgarno, "A review on selective laser sintering/melting (SLS/SLM) of aluminium alloy powders: Processing, microstructure, and properties," *Prog. Mater Sci.*, vol. 74, pp. 401–477, Oct. 2015.

[11] W. F. Smith, *Structure and properties of engineering alloys*. McGraw-Hill, 1993.

[12] W. E. Frazier, "Metal Additive Manufacturing: A Review," *J. Mater. Eng. Perform.*, vol. 23, no. 6, pp. 1917–1928, Jun. 2014.

[13] Y. Li and D. Gu, "Parametric analysis of thermal behavior during selective laser melting additive manufacturing of aluminum alloy powder," *Mater. Des.*, vol. 63, pp. 856–867, Nov. 2014.

[14] T. F. Babuska, B. A. Krick, D. F. Susan, and A. B. Kustas, "Comparison of powder bed fusion and directed energy deposition for tailoring mechanical properties of traditionally brittle alloys," *Manufacturing Letters*, vol. 28, pp. 30–34, Apr. 2021.

[15] M. Agarwala, D. Bourell, J. Beaman, H. Marcus, and J. Barlow, "Direct selective laser sintering of metals," *Rapid Prototyping Journal*, vol. 1, no. 1, pp. 26–36, Jan. 1995.

[16] A. Leis, R. Weber, and T. Graf, "Process Window for Highly Efficient Laser-Based Powder Bed Fusion of AlSi10Mg with Reduced Pore Formation," *Materials* , vol. 14, no. 18, Sep. 2021, doi: 10.3390/ma14185255.

[17] A. J. Sterling, B. Torries, N. Shamsaei, S. M. Thompson, and D. W. Seely, "Fatigue behavior and failure mechanisms of direct laser deposited Ti–6Al–4V," *Materials Science and Engineering: A*, vol. 655, pp. 100–112, Feb. 2016.

[18] R. Snell *et al.*, "Methods for Rapid Pore Classification in Metal Additive Manufacturing," *JOM*, vol. 72, no. 1, pp. 101–109, Jan. 2020.

[19] S. Sun, M. Brandt, and M. Easton, "2 - Powder bed fusion processes: An overview," in *Laser Additive Manufacturing*, M. Brandt, Ed. Woodhead Publishing, 2017, pp. 55–77.

[20] D. Gu, *Laser Additive Manufacturing of High-Performance Materials*. Springer, 2015.

[21] A. E. Wilson-Heid, T. C. Novak, and A. M. Beese, "Characterization of the Effects of Internal Pores on Tensile Properties of Additively Manufactured Austenitic Stainless Steel 316L," *Exp. Mech.*, vol. 59, no. 6, pp. 793–804, Jul. 2019.

[22] N. Read, W. Wang, K. Essa, and M. M. Attallah, "Selective laser melting of AlSi10Mg alloy: Process optimisation and mechanical properties development," *Mater. Des.*, vol. 65, pp. 417–424, Jan. 2015.

[23] F. Trevisan *et al.*, "On the Selective Laser Melting (SLM) of the AlSi10Mg Alloy: Process, Microstructure, and Mechanical Properties," *Materials* , vol. 10, no. 1, Jan. 2017, doi: 10.3390/ma10010076.

[24] D. Buchbinder, W. Meiners, N. Pirch, K. Wissenbach, and J. Schrage, "Investigation on reducing distortion by preheating during manufacture of aluminum components using selective laser melting," *J. Laser Appl.*, vol. 26, no. 1, p. 012004, Feb. 2014.

[25] S. Vock, B. Klöden, A. Kirchner, T. Weißgärber, and B. Kieback, "Powders for powder bed fusion: a review," *Progress in Additive Manufacturing*, vol. 4, no. 4, pp. 383–397, Dec. 2019.

[26] Wohlers Associates and Inc, *Wohlers Report 2017: 3D Printing and Additive Manufacturing State of the Industry : Annual Worldwide Progress Report*. Wohlers Associates, 2017.

[27] C. D. Boley, S. A. Khairallah, and A. M. Rubenchik, "Calculation of laser absorption by metal powders in additive manufacturing," *Additive Manufacturing Handbook*. pp. 507–509, 2017. doi: 10.1201/9781315119106-27.

[28] A. Simchi, "The role of particle size on the laser sintering of iron powder," *Metall. Mater. Trans. B*, vol. 35, no. 5, pp. 937–948, Oct. 2004.

[29] ASTM International, "Test Methods for Flow Rate of Metal Powders Using the Hall Flowmeter Funnel," West Conshohocken, PA, B213-20, 2020. doi: 10.1520/b0213.

[30] J. R. Davis, *Aluminum and Aluminum Alloys*. ASM International, 1993.

[31] A. Aversa *et al.*, "New Aluminum Alloys Specifically Designed for Laser Powder Bed Fusion: A Review," *Materials* , vol. 12, no. 7, Mar. 2019, doi: 10.3390/ma12071007.

[32] X. Liu, C. Zhao, X. Zhou, Z. Shen, and W. Liu, "Microstructure of selective laser melted AlSi10Mg alloy," *Mater. Des.*, vol. 168, p. 107677, Apr. 2019.

[33] L. Thijs, K. Kempen, J.-P. Kruth, and J. Van Humbeeck, "Fine-structured aluminium products with controllable texture by selective laser melting of pre-alloyed AlSi10Mg powder," *Acta Mater.*, vol. 61, no. 5, pp. 1809–1819, Mar. 2013.

[34] T. Minasyan and I. Hussainova, "Laser Powder-Bed Fusion of Ceramic Particulate Reinforced Aluminum Alloys: A Review," *Materials* , vol. 15, no. 7, Mar. 2022, doi: 10.3390/ma15072467.

[35] W. D. Callister, *Materials science and engineering an introduction*. John Wiley, 2007.

[36] D. Herzog, V. Seyda, E. Wycisk, and C. Emmelmann, "Additive manufacturing of metals," *Acta Mater.*, vol. 117, pp. 371–392, Sep. 2016.

[37] M. Krishnan, "Investigation of material and mechanical properties of Al alloy and Al based MMC parts produced by DMLS for industrial application," PhD Thesis. Politec-nico di Torino, 2014.

[38] N. F. En1706, "Aluminium and Aluminium Alloys—Castings—Chemical Composition and Mechanical Properties," *Française de Normalisation, France, Standard No. NF …*, 1706.

[39] D. Manfredi *et al.*, "Additive manufacturing of Al alloys and aluminium matrix composites (AMCs)," in *Light Metal Alloys Applications*, InTech, 2014.

[40] K. Schmidtke, F. Palm, A. Hawkins, and C. Emmelmann, "Process and Mechanical Properties: Applicability of a Scandium modified Al-alloy for Laser Additive Manufacturing," *Physics Procedia*, vol. 12. pp. 369–374, 2011. doi: 10.1016/j.phpro.2011.03.047.

[41] K. Kempen, L. Thijs, J. Van Humbeeck, and J.-P. Kruth, "Mechanical Properties of AlSi10Mg Produced by Selective Laser Melting," *Phys. Procedia*, vol. 39, pp. 439–446, Jan. 2012.

[42] D. Buchbinder, H. Schleifenbaum, S. Heidrich, W. Meiners, and J. Bültmann, "High Power Selective Laser Melting (HP SLM) of Aluminum Parts," *Phys. Procedia*, vol. 12, pp. 271–278, Jan. 2011.

[43] B. J. Mfusi, N. R. Mathe, P. A. I. Popoola, and L. C. Tshabalala, "Influence of stress relieving thermal cycles on AISI10Mg specimens produced by selective laser melting," *IOP Conf. Ser.: Mater. Sci. Eng.*, vol. 655, no. 1, p. 012027, Oct. 2019.

[44] F. Committee and F42 Committee, "Standard for Additive Manufacturing Finished Part Properties Specification for AlSi10Mg with Powder Bed Fusion Laser Beam." doi: 10.1520/f3318.

[45] K. G. Prashanth *et al.*, "Microstructure and mechanical properties of Al–12Si produced by selective laser melting: Effect of heat treatment," *Materials Science and Engineering: A*, vol. 590, pp. 153–160, Jan. 2014.

[46] S. Marola *et al.*, "A comparison of Selective Laser Melting with bulk rapid solidification of AlSi10Mg alloy," *J. Alloys Compd.*, vol. 742, pp. 271–279, Apr. 2018.

[47] *Generative Fertigung von Aluminiumbauteilen für die Serienproduktion - AluGenerativ: Abschlussbericht ; Projektlaufzeit: Februar 2007 - Januar 2010*. 2010.

[48] J. Suchy, L. Pantelejev, D. Palousek, D. Koutny, and J. Kaiser, "Processing of AlSi9Cu3 alloy by selective laser melting," *Powder Metall.*, vol. 63, no. 3, pp. 197–211, May 2020.

[49] J. Forde and W. Stott, "Aluminium-Copper Alloy for Casting," 2534273B1, Oct. 01, 2014

[50] A. McCloskey, "ADDITIVELY MANUFACTURED HIGH-STRENGTH ALUMINUM VIA POWDER BED LASER PROCESSES," 2016/209652 Al, Dec. 29, 2016 [Online]. Available: https://patentimages.storage.googleapis.com/f2/fe/0f/431ca22aee6709/WO2016209652A1.pdf

[51] "A20X Story - Aluminium Casting Alloy, Aeromet International Ltd." https://a20x.com/a20x-story-2/ (accessed Oct. 26, 2020).

[52] A. Aversa *et al.*, "A study of the microstructure and the mechanical properties of an AlSiNi alloy produced via selective laser melting," *J. Alloys Compd.*, vol. 695, pp. 1470–1478, Feb. 2017.

[53] A. B. Spierings, K. Dawson, P. J. Uggowitzer, and K. Wegener, "Influence of SLM scan-speed on microstructure, precipitation of Al3Sc particles and mechanical properties in Sc- and Zr-modified Al-Mg alloys," *Mater. Des.*, vol. 140, pp. 134–143, Feb. 2018.

[54] N. T. Aboulkhair, "Additive manufacture of an aluminium alloy: processing, microstructure, and mechanical properties".

[55] A. T. Sutton, C. S. Kriewall, M. C. Leu, and J. W. Newkirk, "Powder characterisation techniques and effects of powder characteristics on part properties in powder-bed fusion processes," *Virtual Phys. Prototyp.*, vol. 12, no. 1, pp. 3–29, Jan. 2017.

[56] S. Zhang, B. Lane, J. Whiting, and K. Chou, "On thermal properties of metallic powder in laser powder bed fusion additive manufacturing," *J. Manuf. Process.*, vol. 47, 2019, doi: 10.1016/j.jmapro.2019.09.012.

[57] M. Grasso and B. M. Colosimo, "Process defects and in situ monitoring methods in metal powder bed fusion: a review," *Meas. Sci. Technol.*, vol. 28, no. 4, p. 044005, Feb. 2017.

[58] A. Aversa *et al.*, "Single scan track analyses on aluminium based powders," *J. Mater. Process. Technol.*, vol. 255, pp. 17–25, May 2018.

[59] B. A. Fulcher, D. K. Leigh, and T. J. Watt, "Comparison of AlSi10Mg and Al 6061 processed through DMLS," in *Proceedings of the Solid Freeform Fabrication (SFF) Symposium, Austin, TX, USA*, 2014, vol. 46. [Online]. Available: http://utw10945.utweb.utexas.edu/sites/default/files/2014-035-Fulcher.pdf

[60] A. Mortensen and J. Llorca, "Metal Matrix Composites," *Annu. Rev. Mater. Res.*, vol. 40, no. 1, pp. 243–270, Jun. 2010.

[61] I. A. Ibrahim, F. A. Mohamed, and E. J. Lavernia, "Particulate reinforced metal matrix composites — a review," *J. Mater. Sci.*, vol. 26, no. 5, pp. 1137–1156, Mar. 1991.

[62] M. K. Surappa, "Aluminium matrix composites: Challenges and opportunities," *Sadhana*, vol. 28, no. 1, pp. 319–334, Feb. 2003.

[63] S. T. Mavhungu, E. T. Akinlabi, M. A. Onitiri, and F. M. Varachia, "Aluminum Matrix Composites for Industrial Use: Advances and Trends," *Procedia Manufacturing*, vol. 7, pp. 178–182, Jan. 2017.

[64] O. Matvienko, O. Daneyko, T. Kovalevskaya, A. Khrustalyov, I. Zhukov, and A. Vorozhtsov, "Investigation of Stresses Induced Due to the Mismatch of the Coefficients of Thermal Expansion of the Matrix and the Strengthening Particle in Aluminum-Based Composites," *Metals* , vol. 11, no. 2, p. 279, Feb. 2021.

[65] E. Maire, V. Carmona, J. Courbon, and W. Ludwig, "Fast X-ray tomography and acoustic emission study of damage in metals during continuous tensile tests," *Acta Mater.*, vol. 55, no. 20, pp. 6806–6815, Dec. 2007.

[66] P. K. R. J. K. Kim, "Nucleation on Ceramic Particles in Cast Metal-Matrix Composites," *METALLURGICAL AND MATERIALS TRANSACTIONS*, vol. 31A, Apr. 2000, [Online]. Available: https://link.springer.com/article/10.1007/s11661-000-0124-0

[67] P. K. Rohatgi, C. S. Narendranath, S. Ray, and R. Asthana, "Microstructure Formation During Solidification of Metal Matrix Composites, edited by P," *ROHATGI (TMS, 1992)*.

[68] S. Chandrasekaran *et al.*, "Additive manufacturing of graded B4C-Al cermets with complex shapes," *Mater. Des.*, vol. 188, p. 108516, Mar. 2020.

[69] K. Shirvanimoghaddam *et al.*, "Boron carbide reinforced aluminium matrix composite: Physical, mechanical characterization and mathematical modelling," *Materials Science and Engineering: A*, vol. 658, pp. 135–149, Mar. 2016.

[70] I. N. Orbulov, Á. Németh, and J. Dobránszky, "Composite production by pressure infiltration," in *Materials Science Forum*, 2008, vol. 589, pp. 137–142.

[71] R. G. Bhandare and P. M. Sonawane, "Preparation of aluminium matrix composite by using stir casting method," *International Journal of Engineering and Advanced Technology (IJEAT)*, vol. 3, no. 3, pp. 61–65, 2013.

[72] J. M. Torralba, C. E. da Costa, and F. Velasco, "P/M aluminum matrix composites: an overview," *J. Mater. Process. Technol.*, vol. 133, no. 1, pp. 203–206, Feb. 2003.

[73] P. Bishop, "Powder Production Methods."

[74] E. I. Kurbatkina, A. A. Shavnev, and A. V. Gololobov, "A Study of Mechanical Alloying of an Aluminum Composite Material Reinforced with Silicon Carbide Particles," *Met. Sci. Heat Treat.*, vol. 61, no. 5, pp. 295–299, Sep. 2019.

[75] D. K. Koli, G. Agnihotri, and R. Purohit, "Advanced Aluminium Matrix Composites: The Critical Need of Automotive and Aerospace Engineering Fields," *Materials Today: Proceedings*, vol. 2, no. 4, pp. 3032–3041, Jan. 2015.

[76] V. P. Baisane, Y. S. Sable, M. M. Dhobe, and P. M. Sonawane, "Recent development and challenges in processing of ceramics reinforced Al matrix composite through stir casting process: A Review," *International Journal of Engineering and Applied Sciences*, vol. 2, no. 10, 2015, [Online]. Available: https://www.neliti.com/publications/257814/recent-development-and-challenges-in-processing-of-ceramics-reinforced-al-matrix

[77] O. H. Famodimu, M. Stanford, C. F. Oduoza, and L. Zhang, "Effect of process parameters on the density and porosity of laser melted AlSi10Mg/SiC metal matrix composite," *Front. Mech. Eng. Chin.*, vol. 13, no. 4, pp. 520–527, Dec. 2018.

[78] B. AlMangour, *Additive Manufacturing of Emerging Materials*. Springer International Publishing.

[79] J. L. Kennedy, T. D. Drysdale, and D. H. Gregory, "Rapid, energy-efficient synthesis of the layered carbide, Al4C3," *Green Chem.*, vol. 17, no. 1, pp. 285–290, Dec. 2014.

[80] K. Siegert, P. Unseld, J. Baur, F. Kauffmann, E. Arzt, and K. v. Niessen, "Thixoforging of continuous fiber-reinforced AlSi/AlMg-alloys," *Int. J. Mach. Tools Manuf.*, vol. 46, no. 11, pp. 1227–1232, Sep. 2006.

[81] J. S. Nuechterlein and J. J. Iten, "Additive Manufacturing of Metal Alloys and Metal Alloy Matrix Composites," 2018/0161874 A1, Jun. 14, 2018 [Online]. Available: https://patentimages.storage.googleapis.com/a6/29/0a/da156e868e6884/US20180161874A1.pdf

[82] "Data Sheets," *Elementum3d.com*, Feb. 20, 2020. https://www.elementum3d.com/data-sheets (accessed Nov. 02, 2020).

[83] G. A. W. Sweet, M. A. Wells, A. Taylor, R. L. Hexemer, I. W. Donaldson, and D. P. Bishop, "Thermal Mechanical Processing of Press and Sinter Al-Cu-Mg-Sn-(AlN) Metal Matrix Composite Materials," *Metals*, vol. 8, no. 7, p. 480, Jun. 2018.

[84] G. Sweet, "Improving the mechanical and physical properties of an aluminum powder metallurgy metal matrix composite via hot upset forging," Mar. 2019, Accessed: Jan. 17, 2023. [Online]. Available: https://dalspace.library.dal.ca/handle/10222/75208

[85] N. Coniglio and C. E. Cross, "Initiation and growth mechanisms for weld solidification cracking," *Int. Mater. Rev.*, vol. 58, no. 7, pp. 375–397, Sep. 2013.

[86] H. Hyer *et al.*, "Understanding the Laser Powder Bed Fusion of AlSi10Mg Alloy," *Metallography, Microstructure, and Analysis*, vol. 9, no. 4, pp. 484–502, Aug. 2020.

[87] U. Scipioni Bertoli, A. J. Wolfer, M. J. Matthews, J.-P. R. Delplanque, and J. M. Schoenung, "On the limitations of Volumetric Energy Density as a design parameter for Selective Laser Melting," *Mater. Des.*, vol. 113, pp. 331–340, Jan. 2017.

[88] E. Brandl, U. Heckenberger, V. Holzinger, and D. Buchbinder, "Additive manufactured AlSi10Mg samples using Selective Laser Melting (SLM): Microstructure, high cycle fatigue, and fracture behavior," *Mater. Des.*, vol. 34, pp. 159–169, Feb. 2012.

[89] C. Shao, S. Zhao, X. Wang, Y. Zhu, Z. Zhang, and R. O. Ritchie, "Architecture of high-strength aluminum–matrix composites processed by a novel microcasting technique," *NPG Asia Materials*, vol. 11, no. 1, pp. 1–12, Nov. 2019.

[90] A. Aversa *et al.*, "Microstructural and mechanical characterization of aluminum matrix composites produced by laser powder bed fusion: Charcterization of AMCs produced by LPBF," *Adv. Eng. Mater.*, vol. 19, no. 11, p. 1700180, Nov. 2017.

[91] L. C. Astfalck, G. K. Kelly, X. Li, and T. B. Sercombe, "On the breakdown of SiC during the selective laser melting of aluminum matrix composites," *Adv. Eng. Mater.*, vol. 19, no. 8, p. 1600835, Aug. 2017.

[92] D. Gu, Y. Yang, L. Xi, J. Yang, and M. Xia, "Laser absorption behavior of randomly packed powder-bed during selective laser melting of SiC and TiB2 reinforced Al matrix composites," *Opt. Laser Technol.*, vol. 119, p. 105600, Nov. 2019.

[93] M. Balog, P. Krizik, P. Svec, and L. Orovcik, "Industrially fabricated in-situ Al-AlN metal matrix composites (part A): Processing, thermal stability, and microstructure," *J. Alloys Compd.*, vol. 883, p. 160858, Nov. 2021.

[94] D. Dai *et al.*, "Melt spreading behavior, microstructure evolution and wear resistance of selective laser melting additive manufactured AlN/AlSi10Mg nanocomposite," *Surf. Coat. Technol.*, vol. 349, pp. 279–288, Sep. 2018.

[95] D. Dai and D. Gu, "Influence of thermodynamics within molten pool on migration and distribution state of reinforcement during selective laser melting of AlN/AlSi10Mg composites," *Int. J. Mach. Tools Manuf.*, vol. 100, pp. 14–24, Jan. 2016.

[96] F. Rosala, "Improvement and Development of Powder Spreadability Testing," 2021, [Online].

[97] C. N. Hulme-Smith, V. Hari, and P. Mellin, "Spreadability Testing of Powder for Additive Manufacturing," *Berg Huttenmann. Monatsh.*, vol. 166, no. 1, pp. 9–13, Jan. 2021.

[98] A. Liu, C. K. Chua, and K. F. Leong, "Properties of test coupons fabricated by selective Laser Melting," *Key Eng. Mater.*, vol. 447–448, pp. 780–784, Sep. 2010.

[99] E. O. Olakanmi, "Selective laser sintering/melting (SLS/SLM) of pure Al, Al–Mg, and Al–Si powders: Effect of processing conditions and powder properties," *J. Mater. Process. Technol.*, vol. 213, no. 8, pp. 1387–1405, Aug. 2013.

[100] S. Das, "Physical aspects of process control in selective laser sintering of metals," *Adv. Eng. Mater.*, vol. 5, no. 10, pp. 701–711, Oct. 2003.

[101] N. K. Tolochko, Y. V. Khlopkov, S. E. Mozzharov, M. B. Ignatiev, T. Laoui, and V. I. Titov, "Absorptance of powder materials suitable for laser sintering," *Rapid Prototyping Journal*, vol. 6, no. 3, pp. 155–161, Jan. 2000.

[102] P. Mair *et al.*, "Laser powder bed fusion of nano-CaB6 decorated 2024 aluminum alloy," *J. Alloys Compd.*, vol. 863, p. 158714, May 2021.

[103] E. Louvis, P. Fox, and C. J. Sutcliffe, "Selective laser melting of aluminium components," *J. Mater. Process. Technol.*, vol. 211, no. 2, pp. 275–284, Feb. 2011.

[104] T. B. Sercombe and X. Li, "Selective laser melting of aluminium and aluminium metal matrix composites: review," *Mater. Technol.* , pp. 1–9, Mar. 2016.

[105] I. A. Pelevin *et al.*, "AlSi10Mg/AlN Interface Grain Structure after Laser Powder Bed Fusion," *Metals* , vol. 12, no. 12, p. 2152, Dec. 2022.

[106] L. Zhao, J. G. Santos Macías, L. Ding, H. Idrissi, and A. Simar, "Damage mechanisms in selective laser melted AlSi10Mg under as built and different post-treatment conditions," *Materials Science and Engineering: A*, vol. 764, p. 138210, Sep. 2019.

[107] D. Zhang *et al.*, "Grain Refinement of Alloys in Fusion-Based Additive Manufacturing Processes," *Metall. Mater. Trans. A*, vol. 51, no. 9, pp. 4341–4359, Sep. 2020.

[108] N. Takata, H. Kodaira, K. Sekizawa, A. Suzuki, and M. Kobashi, "Change in microstructure of selectively laser melted AlSi10Mg alloy with heat treatments," *Materials Science and Engineering: A*, vol. 704, pp. 218–228, Sep. 2017.

[109] Lv Zhao, Juan Guillermo Santos Macías, Adrien Dolimont, Aude Simar, Edouard Rivière-Lorphèvre, "Comparison of residual stresses obtained by the crack compliance method for parts produced by different metal additive manufacturing techniques and after friction stir processing," *Additive Manufacturing*, Aug. 2020, [Online]. Available: https://www.sciencedirect.com/science/article/pii/S221486042030871X

[110] J. C. Hastie, J. Koelblin, M. E. Kartal, M. M. Attallah, and R. Martinez, "Evolution of internal pores within AlSi10Mg manufactured by laser powder bed fusion under tension: As-built and heat treated conditions," *Mater. Des.*, vol. 204, p. 109645, Jun. 2021.